Cell Reports

Article

From comparative connectomics to large-scale working memory modeling in macaque and marmoset

Graphical abstract

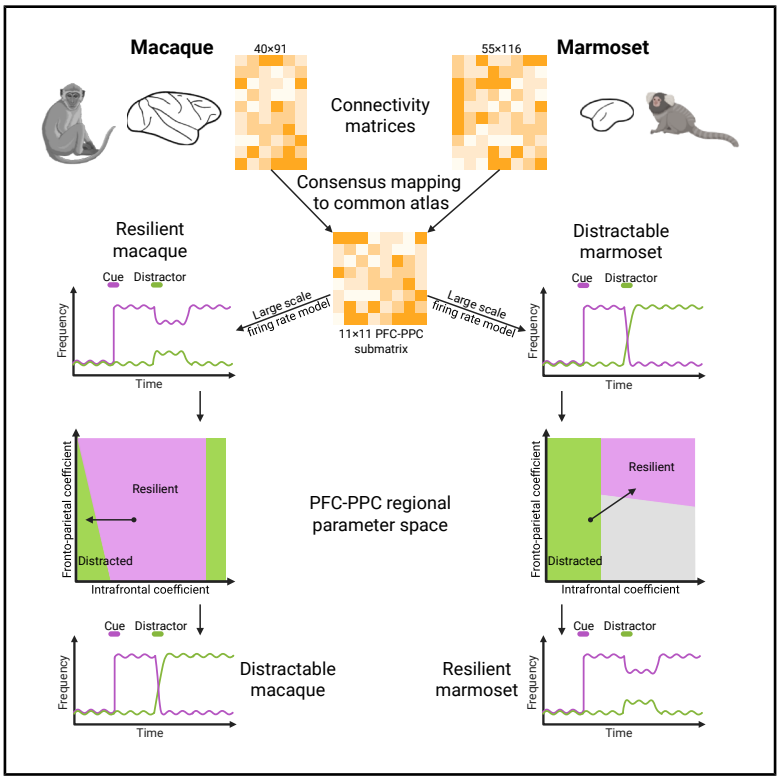

Highlights

- Consensus mapping allows for directly comparing macaque and marmoset connectomes
- Connectomes and spine counts constrain large-scale models of working memory
- The marmoset model is susceptible to distraction, but not the macaque
- Our results capture real-life differences with regard to distraction

Authors

Loïc Magrou, Panagiota Theodoni, Amy F.T. Arnsten, Marcello G.P. Rosa, Xiao-Jing Wang

Correspondence

xjwang@nyu.edu

In brief

After making macaque and marmoset inter-areal connectomes directly comparable through consensus mapping, Magrou, Theodoni, et al. modeled both species using a large-scale model of working memory, which differed only by the two species' anatomy. The model's sensitivity to distraction captures real-life behavioral differences between the two species of primates.

Magrou et al., 2026, Cell Reports *45*, 116847
January 27, 2026
https://doi.org/10.1016/j.celrep.2025.116847

CellPress

Cell Reports

CellPress
OPEN ACCESS

Article

From comparative connectomics to large-scale working memory modeling in macaque and marmoset

Loïc Magrou,[1,2,3,10] Panagiota Theodoni,[4,5,6,7,10] Amy F.T. Arnsten,[8] Marcello G.P. Rosa,[9] and Xiao-Jing Wang[1,11,*]
[1]Center for Neural Science, New York University, New York, NY 10003, USA
[2]Department of Neurobiology, University of Chicago, Chicago, IL 60637, USA
[3]Grossman Center for Quantitative Biology and Human Behavior, University of Chicago, Chicago, IL 60637, USA
[4]Department of Philosophy, National and Kapodistrian University of Athens, 157 84 Athens, Greece
[5]Department of Psychology, Panteion University of Social and Political Sciences, 176 71 Athens, Greece
[6]College Year in Athens, 116 35 Athens, Greece
[7]Faculty of Pure and Applied Sciences, Nicosia 2231, Cyprus
[8]Department of Neuroscience, Yale University School of Medicine, New Haven, CT 06510, USA
[9]Department of Physiology and Neuroscience Program, Biomedicine Discovery Institute, Monash University, Clayton, VIC 3168, Australia
[10]These authors contributed equally
[11]Lead contact
*Correspondence: xjwang@nyu.edu
https://doi.org/10.1016/j.celrep.2025.116847

SUMMARY

Although macaques and marmosets are both primates of choice for studying the brain mechanisms of cognition, they differ in key aspects of anatomy and behavior. Interestingly, a recent connectomic analysis revealed that strong top-down projections from the prefrontal cortex to the posterior parietal cortex, present in macaques and important for executive function, are absent in marmosets. Here, we propose a consensus mapping that bridges the two species' cortical atlases and allows for direct area-to-area comparison of their connectomes, which are then used to build comparative computational large-scale modeling of the frontoparietal circuit for working memory. The macaque model exhibits resilience against distractors, a prerequisite for normal working memory function. By contrast, the marmoset model predicts a sensitivity to distractibility commonly observed behaviorally in this species. Surprisingly, this contrasting trend can be swapped by rescaling intrafrontal and frontoparietal connection weights and offers a credible prediction to the marmoset's behavior in this specific task.

INTRODUCTION

Recent advances in connectomics,[1,2] spanning from local[3–6] to multiregional[7–15] connectivity, offer a novel and quantitative approach to comparisons between species. Comparative work on cortical connectivity has yielded important results in terms of graph theoretical[7,16,17] and scaling[18–21] properties of the brain. However, although structural information is critical, it is often insufficient to predict the dynamical behavior of a recurrent brain system, the understanding of which requires concomitant progress in physiological experiments and computational modeling.[22]

In this context, working memory (WM), the brain's ability to internally maintain and manipulate information in the absence of sensory stimulation, has become a topic of focus, as its representation is distributed across multiple—but not all—brain regions.[23–25] In WM-dependent tasks, neurons in certain parts of the macaque cortex show robust, self-sustained, information-specific, mnemonic persistent activity.[26–29] Experimental observations motivated connectome-based modeling of the macaque monkey cortex for distributed WM.[30,31] Consistent with experimental observations,[32] the frontoparietal network was found to play a major role in WM. Furthermore, a salient characteristic of normal WM is its resilience against distractors,[33–35] whose electrophysiology is now well understood[36–38] and which has been shown in modeling studies to critically depend on the prefrontal cortex (PFC) and its top-down influence on the posterior parietal cortex (PPC) in the macaque monkey cortex.[30,31,39]

Much less is known about the marmoset species, which is rapidly becoming another important animal model in our field.[40–42] Indeed, marmosets possess many of the cognitive attributes of both macaques and humans while at the same time being faster to breed and easier to handle in experiments. Additionally, they possess the same frontoparietal network, known to be the substrate of WM in macaques and humans.[43] They are able to perform WM tasks[44] and have been shown to exhibit sustained delay activity in the PFC during those tasks.[45] Finally, the recent publication of the most complete retrograde-tracer-based marmoset connectome available to date[7,8] allows for analysis and comparison with the macaque.

Although marmosets can perform such tasks, they are harder to train,[46] overall less capable of holding items in WM,[47] and remain significantly more distractible than macaques.[48] Through this convergence of anatomical, functional, and behavioral evidence, we find ourselves with the unique opportunity to push forward the comparative method into the realm of computational neuroscience. We can now apply the same model to both species, knowing that any behavioral difference that might emerge will be solely due to the differences in anatomy. Specifically, differential distractibility could be captured with adequate modeling.

We will first provide a common anatomical framework for the two species, which we have named ''consensus mapping,'' whose purpose will be to reduce the macaque and the marmoset independent atlases to a common parcellation scheme where areal connectivity can be compared directly and then convert all the available anatomical data to it, connectivity and spine count gradient alike. Second, we will constrain an otherwise identical model with those two sets of now one-to-one comparable anatomical data and investigate commonalities and differences in the model's behavior.

RESULTS

Marmosets lack key frontoparietal feedback from 46d_9/46d

The atlases of macaque and marmoset hold 91 and 116 areas before consensus, respectively, with 40 and 55 injected areas (Figures 1A and 1B, injected areas are in bold). Consensus brings the two atlases to 74 areas on both sides, capitalizing on primate analog broader areas. Applying consensus to connectivity itself, the number of injected areas is now 35 for the macaque and 45 for the marmoset. Of these, 29 are common to both species (Figures 1C and 1D, injected areas are in bold).

The 29 $\times$ 29 square consensus connectivity matrices (Figures 1E and 1F) comprise 794 and 809 connections for the macaque and the marmoset, respectively, over 29 $\times$ 28 = 812 possible connections (self-connections are ignored), leading to respective graph densities of 0.68 and 0.72. For the macaque, the distribution of $log_{10}FLN$ (fraction of labeled neurons; i.e., connection weights) is best approximated by a normal distribution, with a mean of -2.60, vs. -2.28 in the marmoset, which is consistent with previous results from Theodoni et al.[7] in spite of modifications produced by the consensus (Figure 2A). Also consistent with previous works, if the macaque spans the usual 6 orders of magnitude,[13,49] the marmoset spans only 5 of them.[7,8] The correlation between macaque and marmoset $log_{10}FLN$ data is 0.59. Notably, the marmoset lacks some of the top-down connections from the dorsal lateral PFC (DLPFC) to the PPC that the macaque has, from area 46d_9/46d to the LIP, which is a major contributor to spatial WM in the macaque. Conversely, the macaque appears to be missing some—albeit weak—connections from area 10 (A10) to the medial parietal and posterior visual areas, suggesting that A10 in the marmoset may retain some features of the more posterior prefrontal areas, such as the frontal eye field (A8aD_A8aV) (Figure 1F).

Macaque connectivity is, on average, more feedback, while marmoset somato-motor areas are higher up in the cortical hierarchy

Correlation is weaker in terms of SLN (supragranular labeled neuron; Figure 2B, $r = 0.32$). Further, the macaque average is lower ($\mu = 0.47$) than that of the marmoset ($\mu = 0.59$), meaning that macaque connections tend to be, on average, more feedback (FB; originating in infragranular layers), whereas the marmoset is tendentially more feedforward (FF; originating in supragranular layers; Figure S5), consistent with the non-consensus original data.[7,8] Figure 2C shows the difference in SLN-based hierarchical estimates[14,50] for the two species, with areas ordered on the macaque hierarchy. The marmoset consensus areas A3a_A3b (primary somatosensory for touch and proprioception), A4ab_A4c (primary motor or M1), A1-2 (primary somatosensory for texture, size, and shape), and PE_PEC (somatosensory dedicated to forelimb digits and joints, which also receives direct somatosensory thalamic inputs[51]) have higher hierarchical values than their macaque counterparts (macaque areas 3, F1, 1_2m, and 5, respectively). This, again, is consistent with the pre-consensual data.[7] In other words, somatosensory and M1 modalities are higher in the global cortical hierarchy in the marmoset than they are in the macaque. At the top of the marmoset hierarchy is consensus area A6Va_A6vb (macaque consensus area 44_F5, a motor oro-facial homolog to Wernicke in humans).

Conversely, the marmoset prefrontal areas A45, A9, A47 (macaque area 12), and A10 have lower hierarchical values than their macaque counterparts. Other interesting differences also occur in the visual system, such as the marmoset areas V4, OPt, and MIP (V4, DP, and MIP in the macaque), which also display higher hierarchical estimates. Thus, sensory-motor areas are tendentially higher in the hierarchy for the marmoset, while more associative areas tend to be higher in macaques.

Marmosets show lower spine count values compared to macaque

Spine counts have been shown elsewhere to correlate positively with SLN-based hierarchy in macaques.[30,52] Here, we show that the marmoset species also displays a correlation of spine count with hierarchy, albeit different in slope (Figure 2D). This is yet again consistent with pre-consensus data,[7] thus further validating that the consensus process conserves properties well. In the current consensus data, the maximum is just short of 5,000, whereas macaque maximal values go beyond 8,000. This may be due to a lack of data, but available data for homolog areas in both species suggest a genuine difference (see the marmoset areas A9, A10, TEO, and TE3 and the respective macaque counterparts).

Macaque and marmoset have different optimal global couplings

Because the 11 $\times$ 11 model does not contain primary sensory areas, both cues (always in excitatory population A) and distractors (always in excitatory population B; Figure 3D) are sent to all parietal areas, so as to reflect the distributed input those areas should normally receive from the early visual system.

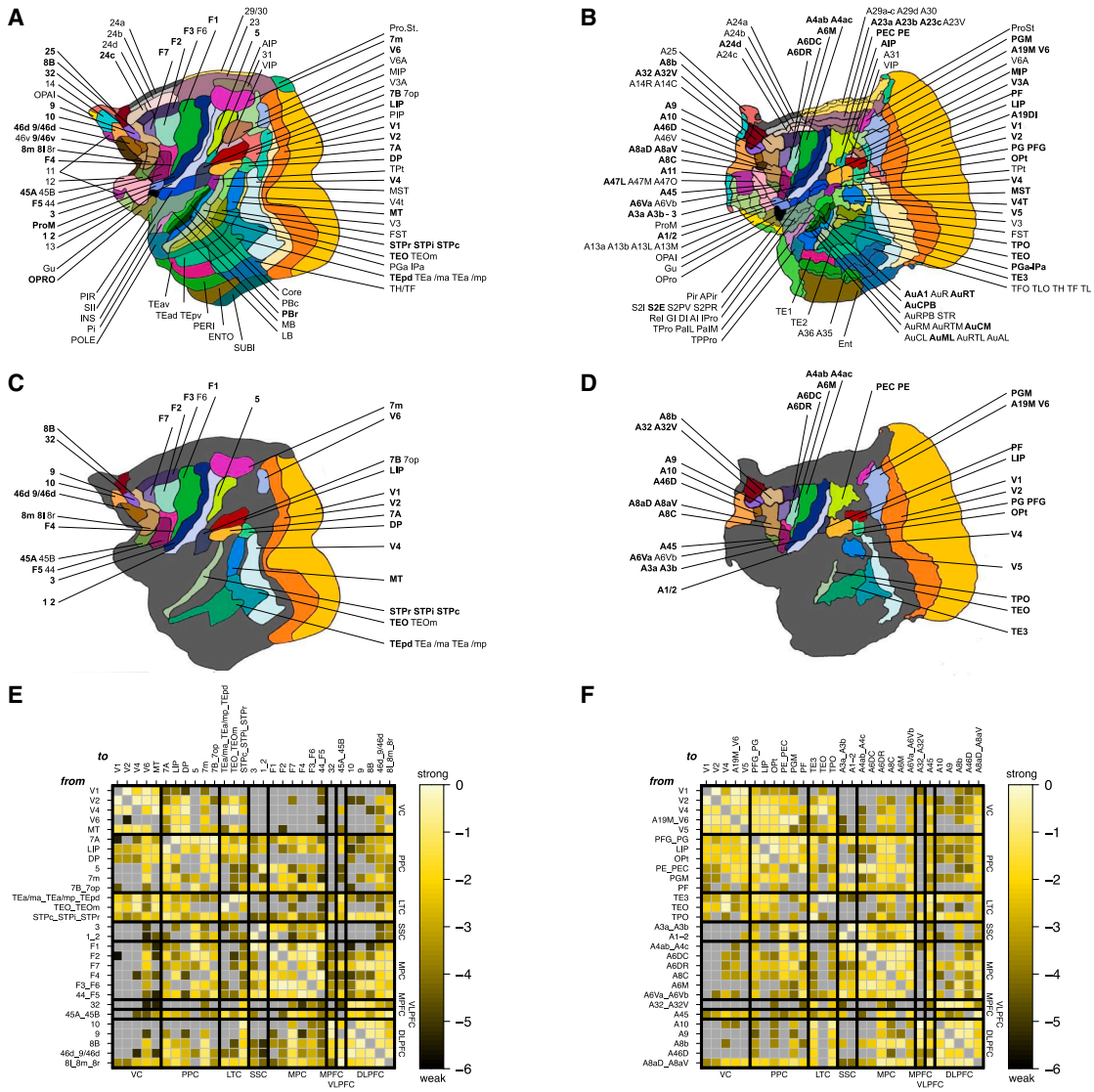

Figure 1. Flatmaps and 29 × 29 $\log_{10}$*FLN* matrices of consensus mapping

(A) Macaque original 91 area atlas from Markov et al.[13]

(B) Marmoset original 116 area atlas from Theodoni et al.[7]

(C) Macaque 29 consensus areas commonly injected with the marmoset.

(D) Marmoset 29 homolog consensus areas from (C) commonly injected with the macaque.

The area names placed on the same line represent areas that will be aggregated as one area by the consensus mapping and are shown as separate areas of identical color in (A) and (B) and then fused in (C) and (D). The names in bold are those for which there was at least one injection by the original connectivity dataset. For ease of reading, area labels are identically ordered between macaque (A and C) and marmoset (B and D). The full table of consensus equivalence across the two species is available in Table S3.

(E and F) The 29 × 29 common consensus $\log_{10}$*FLN* matrices for macaque and marmoset, respectively. Each square of color represents a connection from source areas as rows to target areas as columns. Colors vary according to $\log_{10}$*FLN* values, from very weak (black) to very strong (bright yellow). Gray is the background color of the matrices, and a gray square therefore identifies an absent connection. Thicker black lines separate brain regions; see Table S3 for a key to regional acronyms. Areas merged by consensus are labeled by concatenating the names of the original parcellation areas, separated by an underscore. Thanks to consensus, each connection is here one-to-one comparable across species. The corresponding SLN matrices are available in Figure S4, and a comprehensive connectivity table with both FLN and SLN values can be found in Table S3.

Additionally, only a combination of 4–5 parietal areas (depending on the selected areas) achieves the goal of distributed sustained activity. Cues are always sent 1 s into the simulation and distractors at 4.5 s. Finally, population A and B stable points are identical in terms of firing rate values, as already established in Mejias and Wang.[30]

All free parameters of this model are fixed at the same values for both species, except for the global coupling

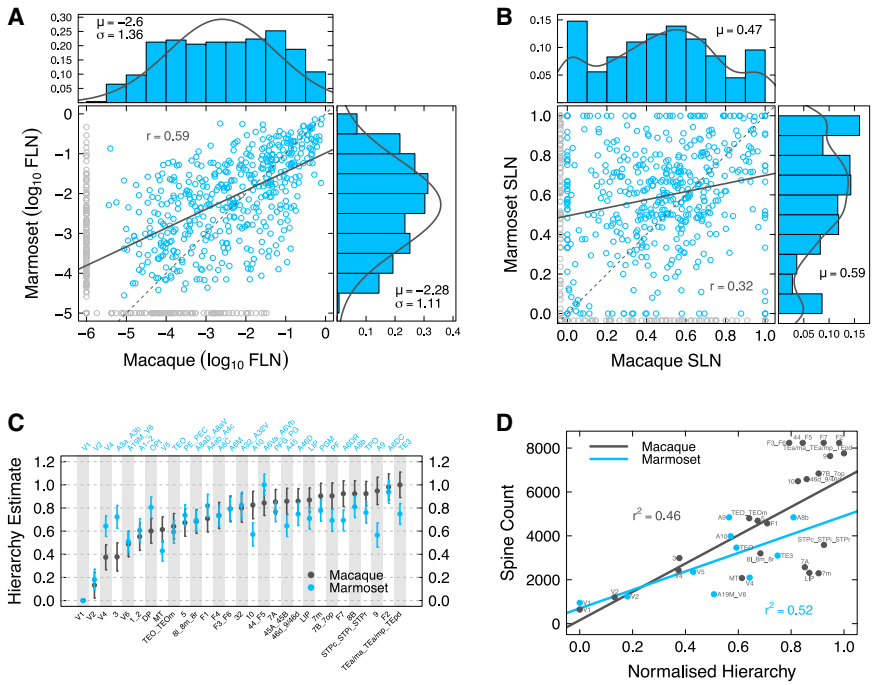

Figure 2. 29 × 29 connectome statistics, SLN-based hierarchy estimates, and spine counts

(A) Macaque (horizontal axis) vs. marmoset (vertical axis) consensus $log_{10}FLN$ correlation and distribution. In the main plot, each circle represents a connection. Blue, the connection exists in both species; gray, the connection exists in only one species. Solid black line, linear regression line between macaque and marmoset $log_{10}FLN$s, excluding gray datapoints; correlation coefficient of the regression line $r = 0.59$; thin broken line, line of unit slope for visual reference. In the top plot is the $log_{10}FLN$ distribution for the macaque, including connections unique to the macaque; mean $\mu = -2.6$ and standard deviation $\sigma = 1.36$ are used as parameters for the superimposed black normal curve. The same statistics are shown in the left plot for the marmoset, and the same conventions apply.

(B) Macaque (horizontal axis) vs. marmoset (vertical axis) consensus SLN correlation and distribution. The same reading conventions as in (A) were used.

(C) SLN-based hierarchical estimates for macaque (black dots) and marmoset (blue dots), computed by a generalized linear model (GLM) of the beta-binomial family using a logit link function. Error bars represent standard error (SE). Values are ordered by macaque increasing estimates. Bottom axis, macaque consensus areas; top axis, marmoset homolog consensus areas.

(D) Spine count as a function of normalized SLN-based hierarchy. Black dots and regression line, macaque; blue dots and regression line, marmoset. The proportion of variance explained r^2 is 0.46 for the macaque and 0.52 for the marmoset.

parameter *G*, which requires specific parametrization for each species to meet certain basic behavioral criteria: (1) being able to produce distributed and sustained activity and (2) not to produce spontaneous sustained activity if not solicited by a cue.

We determined the valid range of *G* values by doing a systematic parameter search with a gradual incrementation of step size 0.01 for both species, using 10 s simulations over 20 different random seeds (Figure 4A). The average valid range of value goes from 0.80 to 1.16 in the macaque, vs. from 0.57 to 1.13 in the marmoset. Final values of *G* (Figure 4A) were chosen as the mid-point of the resilient range for the macaque (0.98) and the distractible range for the marmoset (0.85). Specific to the macaque system is the existence of a regime of partially resilient behavior (from 0.45 to 0.80), where prefrontal areas show persistent activity but parietal areas fail to do so (Figure 4B; a complete set is shown in Figure S6A). Additionally, there exists a small, non-robust window of low *G* values (between 0.50 and 0.57) that produces a resilient marmoset (Figure 4C; a complete set is shown in Figure S6B).

The macaque is resilient to distraction, not the marmoset

With *G* now fixed, both species in the 11 × 11 model achieve distributed sustained activity throughout the system prior to distraction (Figure 5, purple trace), as is expected from a number of previous works.[26–29,33,44,45] Note the very low rate of areas DP and 8l_8m_8r in the macaque compared to their marmoset equivalents, OPt and A8aD_A8aV. After sending the distractor in excitatory population B, the macaque shows a resilience to distraction (Figure 5A, purple trace) after a brief transient collapse of cue encoding in the PPC (Figure 5A, green trace), consistent with single-cell LIP[36,54] and VIP[55] recordings. Additionally, PFC areas are able to maintain their activity in spite of the distractor affecting the PPC areas, encapsulating known results.[33,37,38] In opposition to this, the marmoset's population B takes over (Figure 5B, green trace), thus predicting that distractor encoding activity would propagate to the DLPFC in marmosets. Further, macaque area DP and consensus area 8l_8m_8r (i.e., the FEF) fail to achieve strong activity, contrary to their marmoset counterparts, OPt and A8aD_A8aV (marmoset FEF).

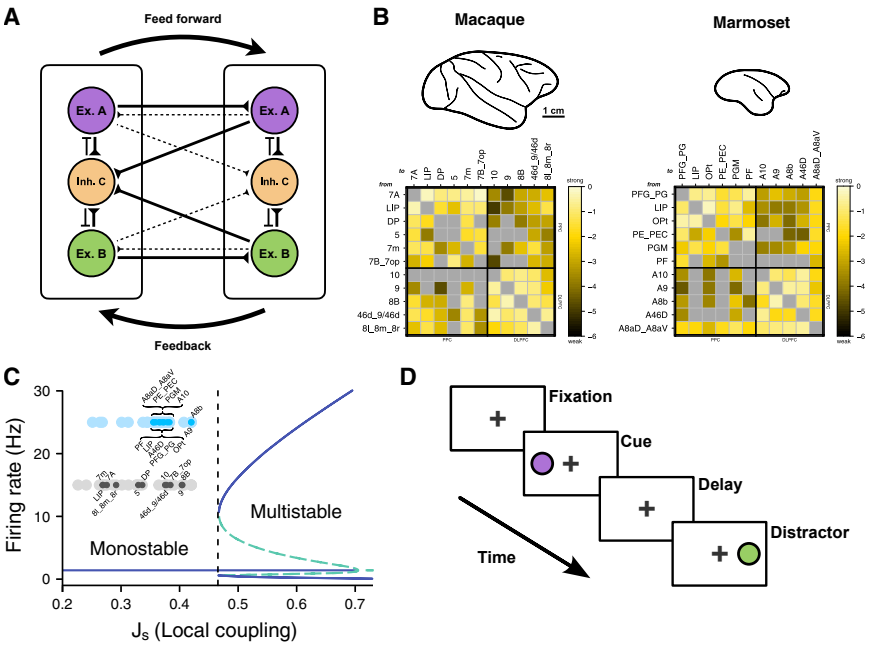

Figure 3. Large-scale model of distributed working memory

(A) Schematic of the local circuit and inter-areal interactions. The local circuitry follows a standard 3-population Wong and Wang model,[53] with 2 excitatory populations (ex. A and ex. B, purple and green) and 1 inhibitory population (inh. C, orange). Locally, populations A and B excite population C, which inhibits them in return; globally, inter-areal interactions are based on FLN and SLN anatomical data.

(B) Comparative visual showing the macaque and marmoset brains at the same scale; scale bar, 1 cm. Bottom, the 11 × 11 submatrices that will be used for WM modeling. PPC, posterior parietal cortex; DLPFC, dorsal lateral prefrontal cortex. Reading conventions are identical to those used in Figures 1E and 1F.

(C) Bifurcation diagram for an isolated area, with firing rates (Hz) as a function of parameter J_s. Below a certain threshold value of J_s, a single area cannot sustain long-term activity and is monostable. Areas are all parametrized to fall below that threshold. Small dark gray dots correspond to each of the 11 macaque areas from (B) and indicate their particular J_s values, while larger pale gray dots represent the distribution of the rest of the 29 common consensus areas. Regular and pale blue dots assume the same function with respect to the marmoset.

(D) Schematic representation of the WM task time course. After a 1 s fixation period, the cue is presented for 0.5 s (purple disk) in the form of a pulse of 0.3 nA sent to population A. After a delay period of 3 s, the distractor is presented (green disk) as a pulse to population B, identical in time and intensity to the cue.

This difference is not dependent on parametrization and can be explained by the fact that macaque FEF receives less cumulative parietal inputs and more prefrontal inputs than marmoset FEF (Figure 2B; a detailed explanation is provided in the supplemental text). The same observation is true for macaque area DP compared to its marmoset homolog, OPt. Adding to this the fact that connections to both macaque FEF and DP are more FB than in the marmoset and therefore more inhibitory via the counter-inhibitory bias (CIB; see Mejias and Wang[30]), we see that the anatomy easily explains the dynamical difference between the two species.

Additional simulations were run with a 2 × 2 PFC-PPC model on the one hand and a full 29 × 29 area on the other. The 2 × 2 model shows a similar tendency to that of the 11 × 11, with the

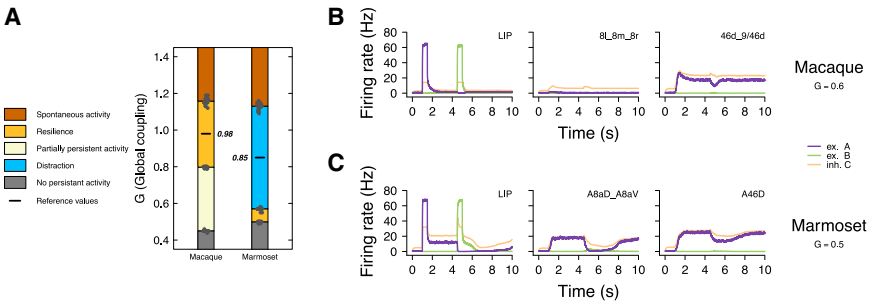

Figure 4. Parametrization of global coupling parameter *G*

(A) Stacked histogram showing different regimes of activity as a function of *G*, for both species. Dark orange, spontaneous activity; yellow, resilience to distraction; pale yellow, partially persistent activity; blue, distraction; dark gray, no persistent activity; black line, reference (chosen) value. Simulations were run with incremental *G* steps of 0.01, with 20 different random seeds (black dots). Boundaries between regimes are computed as averages over all seeds at each qualitative change of regime. The reference value for each species is defined as the half point in the resilience regime for the macaque and the distracted regime for the marmoset.

(B) Firing rate as a function of time for the macaque's partially persistent regime at $G = 0.6$. Purple trace, excitatory population A; green trace, excitatory population B; orange trace, inhibitory population C. Areas have been selectively chosen to showcase the partialness of this regime, with parietal areas not sustaining activity (LIP), while prefrontal areas do (46d_9/46d). Consensus area 8l_8m_8r (FEF) is shown as the one prefrontal area that does not follow this logic.

(C) Example behavior for the marmoset's small window of resilient regime at $G = 0.5$, where population A re-establishes itself after the distractor pulse. Homolog consensus areas and reading conventions are the same as those in (B).

A complete set for (B) and (C) is available in Figures S6A and S6B.

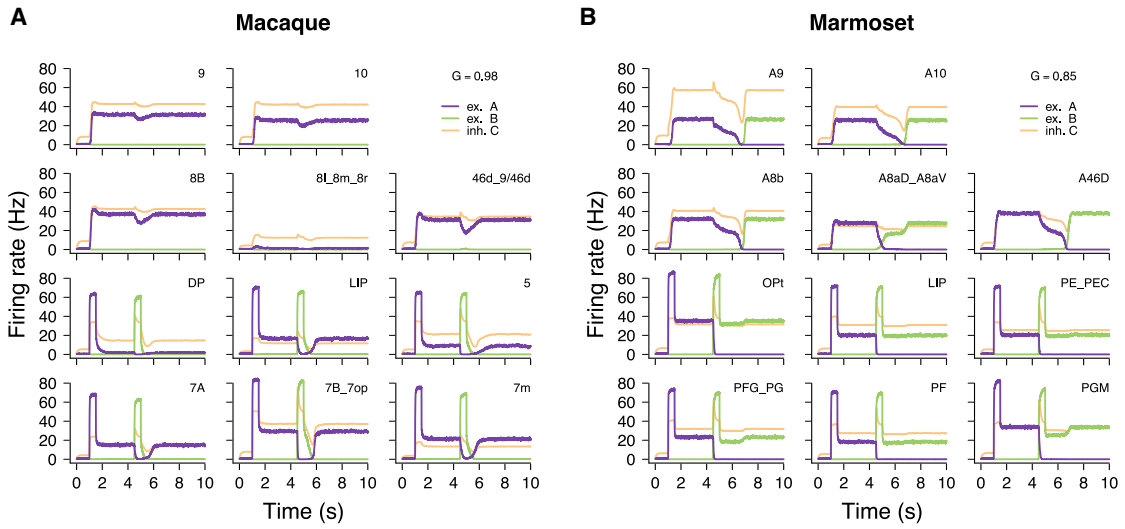

Figure 5. Standard behavior of the distributed frontoparietal working memory model

Each subplot shows the activity traces of the firing rates as a function of time for each of the 11 consensus areas of the selected frontoparietal network. Areas are directly comparable with their homolog and are placed accordingly. Cues (t = 1 s to population A, purple trace) and distractors (t = 4.5 s to population B, green trace) are sent to all parietal areas. The orange trace is inhibitory population C.

(A) Macaque; global coupling parameter G = 0.98, resilient regime.

(B) Marmoset; G = 0.85, distractible regime.

macaque being resilient and the marmoset being partially (but not completely) distractible (Figures S7A and B). The 29 × 29 version of the model fails to yield the same species difference (Figures S7D and E).

Changes in regional coupling can reverse resilience and sensitivity

In order to understand what makes the macaque and the marmoset different in their distractibility, we investigated how we could make the macaque model susceptible to distraction and force the marmoset to be resilient. "Grafting" the macaque-specific connections to the marmoset, and vice versa, failed to yield the expected result (Figure S8). We therefore elected to divide the 11 × 11 connectivity matrices of both species into 4 quadrants, akin to intra-regional and inter-regional subsets of connections, and attributed to each a specific multiplicative parameter, from ρ_1 to ρ_4 (Figure 6A). The parameter space of ρ_1 vs. ρ_2 is shown in Figure 6B. Conversion can be achieved in the macaque by reducing ρ_1 to any value below 0.6 (Figure 6A; this is also true for the 2 × 2 PFC-PPC macaque model; see Figure S7C), thus effectively tuning down the intrafrontal connectivity and shifting the system to a part of the parameter space where distraction can occur (Figure 6B, left, leftward arrow). Sensitivity to distraction in the macaque can be observed for a selection of example areas in Figure 6C (a complete set is provided in Figure S9A).

As can be seen in Figure 6B, the macaque possesses what appears to be another distracted territory for very high values of ρ_1, with a gradual transition roughly centered around 1.8. However, this part of the parameter space is in fact unstable, as the outcome behavior depends on the random seed used. This is indicative of a parameter going beyond its realistic limits. At these levels, any random fluctuation is amplified by a factor of close to 2 in the prefrontal areas. Helped by a higher firing rate baseline, also due to the higher ρ_1 value, this leads to an easy propagation to the rest of the network. Due to its unrealistic nature, this will not be discussed further in what follows.

A marmoset resilient to distraction can similarly also be achieved by giving ρ_1 and ρ_2 a value of at least 1.4 each (Figure 6C), which effectively displaces the system to a part of the parameter space that grants it resilience (Figure 6B, right, right-upward arrow), with example areas showcasing the behavior in Figure 6C (a complete set is shown in Figure S9B). A mixed behavior regime exists in the marmoset's ρ_1-ρ_2 plane, which is characterized by partial activations in the system (Figure S9C). The 2 × 2 PFC-PPC marmoset model effectively sits in this regime. Consistently, a single change of ρ_2 to 1.7 pushes the 2 × 2 system upward into resilient territory (Figure S7C).

Similar parameter spaces can be achieved with ρ_3 and ρ_4, and are topologically similar to the ones of ρ_1 and ρ_2 (Figure S10C). There, the macaque becomes sensitive to distraction as one increases ρ_4, and the marmoset becomes resilient as both ρ_3 and ρ_4 are reduced. For practical purposes, the focus will be on ρ_1 and ρ_2 in what follows.

Gradual changes in regional coupling indicate a sharp transition between resilient and distracted regimes

The next logical step was to understand the transition from one regime to the other. To do so, we performed simulations at incremental steps of ρ_1, across the border that separates the two regimes, and looked at the conductance S_A-S_B phase space (i.e., the S variables of excitatory populations A and B) for the system's trajectories, using 10 different random seeds each time. For the macaque, ρ_2 was fixed at a value of 1, and ρ_1

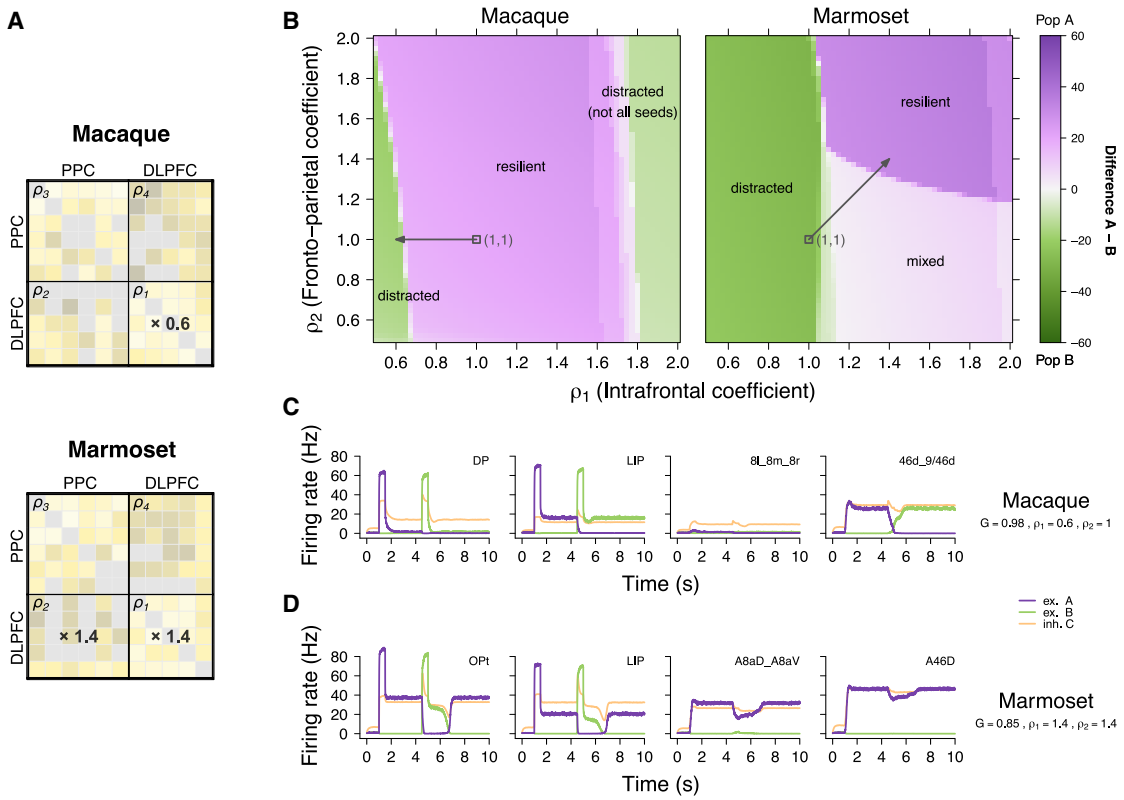

Figure 6. Parameter space analysis of resilience and distractibility

(A) 11 × 11 matrices from Figure 3B divided into four quadrants: ρ_1, DLPFC to DLPFC or intrafrontal; ρ_2, DLPFC to PPC or frontoparietal; ρ_3, PPC to PPC or intraparietal; and ρ_4, PPC to DLPFC or parietofrontal. Setting ρ_1 to 0.6 in the macaque makes it sensitive to distraction. Setting ρ_1 and ρ_2 to 1.4 in the marmoset makes the system resilient.

(B) ρ_1-ρ_2 parameter plane for both macaque (left) and marmoset (right). Green hues indicate resilient territories in the plane, purple hues indicate distracted, and white indicates mixed behavior (see Figure S6C). Each square is the average of simulations performed over 10 different random seeds by incremental steps of 0.025 in both directions. Open black squares indicate (1,1) coordinates in the plane, and black arrows indicate the displacements generated by the values in (A).

(C) Example behavior for the macaque's distractible regime at G = 0.98, ρ_1 = 0.6, and ρ_2 = 1.

(D) Example behavior for the marmoset's resilient regime at G = 0.85, ρ_1 = 1.4, and ρ_2 = 1.4. Reading conventions are the same as those used in Figures 4B and 4C. A complete set for (C) and (D) is available in Figures S9A and S9B.

varied from 0.75 to 0.55 (i.e., from resilient to distractible) with a step size of 0.01 (Figure 7A, ρ_1-ρ_2). Figure 7A displays the state of the macaque S_A-S_B phase portrait (rotated by $\pi/4$) for increasing values of ρ_1. At ρ_1 = 0.72 (first image on the left, with a full progression visible in Video S1), the macaque displays its standard behavior. The at-rest stable fixed point (black dot) is quickly reached (black trajectory originating from coordinate (0,0)), and the system will stay there until the cue is delivered. Sent to either population A (purple trajectory) or population B (green trajectory), the cue pushes the system to the stable fixed point specific to the population that was cued (a purple point for population A and a green point for B), albeit after a quick overshoot. A distractor, injected in the opposite population, forces the system's trajectory to shoot inward for the duration of the pulse (yellow and red trajectories), only to fall back to the stable fixed point at which they were before distraction.

Trajectories will become increasingly tempted by the other side as ρ_1 decreases. Transition into the distractible macaque occurs over a very narrow band of ρ_1 values, contained between 0.64 and 0.63, at which point independent random seeds show radically different trajectories, with some returning to their fixed point of origin and others ending their course on the opposite stable fixed point. From ρ_1 = 0.62 downward, the system has fully transitioned to being distractible, and all seeds display similar behavior once again, this time to be diverted to the opposite fixed point.

Looking now at the marmoset, we followed an identical procedure, except fixating ρ_2 at a value of 1.5 so as to avoid going through the mixed regime of behavior (Figure 7B, ρ_1-ρ_2). ρ_1 was set there to vary this time from 0.975 to 1.175, again with steps size of 0.01. At ρ_1 = 0.985, well before the transition happens, trajectories are qualitatively analogous to those of the distractible macaque. As ρ_1 progresses toward the threshold of behavioral shift, random seed trajectories remain well grouped together and will remain so during and after the transition, which is an interesting difference from the macaque, arguing for a qualitatively different high-dimensional landscape, as they might in

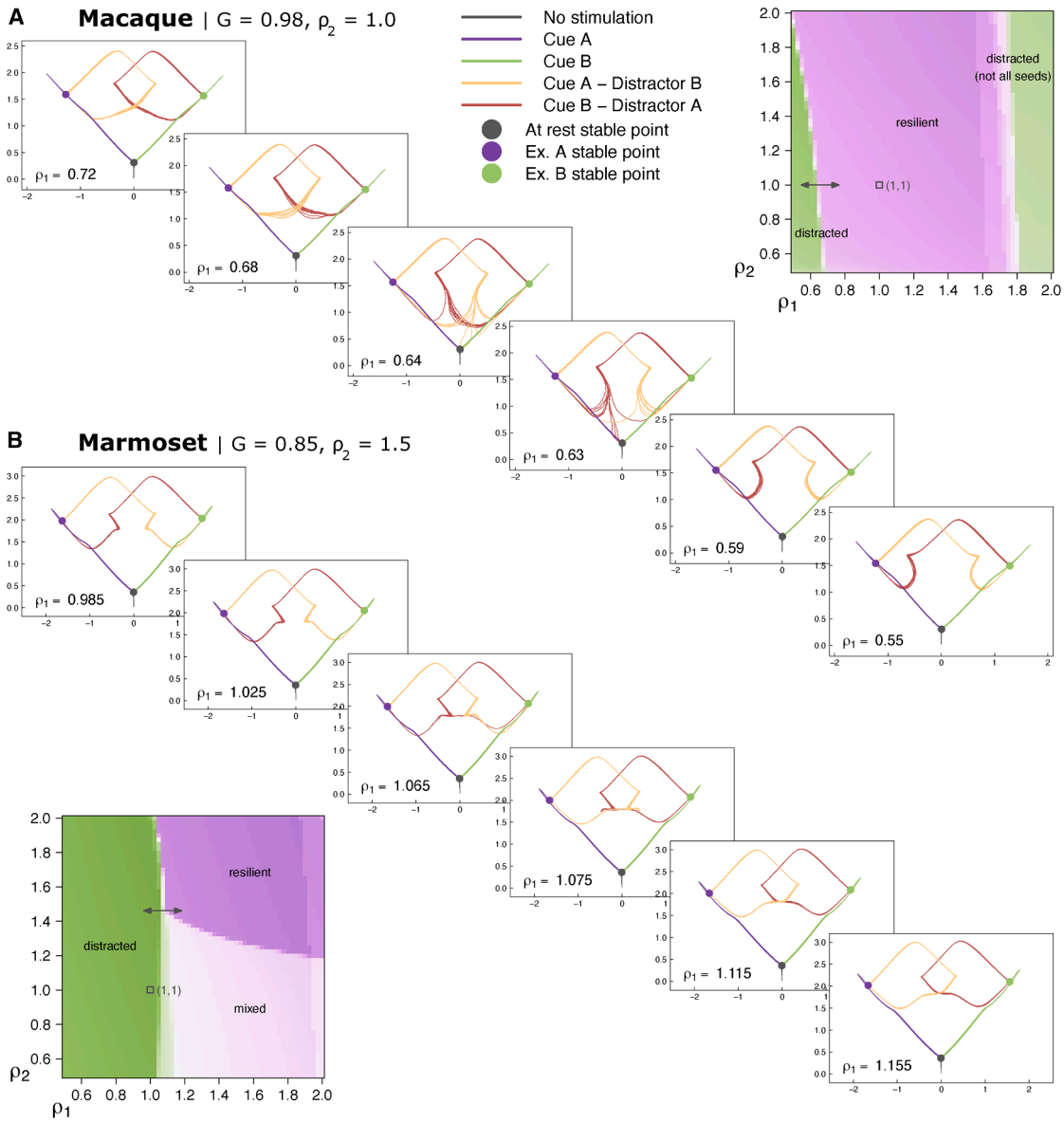

Figure 7. S_A-S_B conductance phase space gradually changes across regime boundaries

The plane is chosen as the unique plane defined by the 3 stable fixed points of the system and then rotated by $\pi/4$ for visual clarity. Colored dots indicate said fixed points: black, at rest (no input current); purple, population A; green, population B. Colored lines follow the same convention for trajectories: black, at rest (no input current); purple, cue input current in population A; green, cue input current in population B; yellow, distractor input current in population B when at stable fixed point A; dark red, distractor input current in population A when at stable fixed point B. Trajectories were computed for 10 different random seeds for all conditions.

(A) Macaque. Each plot corresponds to an incremental step in ρ_1, starting from a resilient macaque. Parameters G and ρ_2 are fixed at 0.98 and 1, respectively. The full investigated range is from $\rho_1 = 0.75$ to $\rho_1 = 0.55$ with a 0.01 step size, available in Video S1A.

(B) Marmoset. Each plot corresponds to an incremental step in ρ_1, starting from a distractible marmoset. Parameters G and ρ_2 are fixed at 0.85 and 1.5, respectively. The full investigated range is from $\rho_1 = 0.975$ to $\rho_1 = 1.175$ with a 0.01 step size, available in Video S1B. For each species, inset plots help visualize the covered range of values in the ρ_1-ρ_2 parameter space.

fact be fanning out in a different plane. The transition itself is even shorter than in the macaque, as all seeds have transitioned at $\rho_1 = 1.075$ to a fully resilient marmoset. Interestingly, trajectories still show a small detour along their former distractor-sensitive path before turning around toward their newly found target. The last of this can be seen at $\rho_1 = 1.105$ (Video S2).

DISCUSSION

Consensus mapping conserves statistics and is a great tool for future comparative work

The consensus mapping exposed here offers the unique opportunity to directly compare the mesoscale connectomes of two

species of primates. Allowed by the extensive anatomical analogies that exist between primates, the consensus mapping is largely based on the merging of subareas to recover coarse-grained, well-established areas, albeit with some loss in spatial granularity for either species. Nonetheless, as we have seen in Figures 2 and S5, the consensus process conserves the basic statistics, FB and FF distributions, graph densities, and spine count-to-hierarchy relationship[7,17,20] of each species pre-consensus. Therefore, the mapping is stable enough to be meaningful for the modeling depicted in this study. Future anatomical investigations of these two species will continue to improve the overlap of injected areas and should prove important for future comparative work in primate anatomy.

Distractibility is intrinsic to the marmoset model

As we have shown, the macaque and marmoset models, which are identical except for their anatomical data, capture an important difference between the actual species in their resilience to distraction. If this result is consistent with known macaque capabilities and electrophysiology,[26–29,33] marmoset research is still at too early a stage to confirm our prediction, although available results are certainly consistent with our finding.[44,45,48]

In the macaque, the parametrization of the global coupling parameter G (Figure 4A) is fairly straightforward. There exists only one bracket of values that produce a fully distributed activity without running the risk of a spontaneous one, with no value leading to a distractible system. The marmoset, on the other hand, although its largest window of viable activity is indeed the distractible one, does have a valid, if narrow and less robust, window of resilient behavior. Therefore, purposefully choosing a distractible G value to then claim that our model captures differential distractibility may appear self-fulfilling. However, that would be missing the point, which is that the macaque possesses no distractible G values when the marmoset is mostly distractible for the same range of values, thus giving vastly different resilience/distractibility profiles as a function of G. Distractibility in the marmoset is therefore a strong prediction of our modeling, softly confirmed by the 2×2 modeling. The only difference is that the marmoset defaults to the mixed behavior regime, but it is still very much closer to distraction than the macaque. Given that the models differ by anatomy only, this G profile difference can only be attributed to the variations in anatomy across the species. This means that a network-distributed, complex-system effect from structure to function is at work here, as no single change in the connectivity matrix can produce this behavioral difference on its own. A second aspect of parametrization concerns the parameters J_s and J_{IE}, which, albeit fixed for each area, will vary as a function of the available spine count gradient data.

As shown earlier, the 29×29 version of the marmoset model fails to achieve distractibility (Figures S7D and S7E), and this begs the question of why the 11×11 subnetwork effectively captures the species difference when the 29×29 does not. There is a growing understanding that different brain states, such as sleep, wakefulness, attention, vision, relaxed mind wandering, and, indeed, WM, have network counterparts of specifically active and synchronized cortical areas,[56–58] while others tend to desynchronize for the duration of that state, as seen in state transitions.[59] Selecting for the WM network[26,32] in this study is meant to be an analog of the brain being in that specific state. To recover the result while keeping the full 29×29 network would require modeling state transitions by implementing a modulatory mechanism that gates out the other areas, potentially based on neurotransmitters such as dopamine[48,60] or other modulatory systems.[31]

A larger brain increases feedbackness and therefore stability and resilience to distraction

The very low level of activity in the macaque FEF and DP, compared to their marmoset counterparts, can be explained by the difference in connectivity for these areas across the two species. As we have argued elsewhere,[18] these anatomical differences can be thought of in the framework of the scaling properties of the brain. Indeed, due to physical constraints exerted on the brain,[61] a bigger brain will get bigger only at the cost of reducing its overall connectivity, which in turn leads to an increasing modularity of its network.[18,62] This scaling effect may well be at work: the macaque and the marmoset 29×29 consensus connectivity matrices in Figures 1E and 1F have similar graph densities, although a 4% drop is already detectable from the marmoset (0.72) to the macaque (0.68). Additionally, Figure 2A clearly shows that the macaque's FLN range spans 6 orders of magnitude, while that of the marmoset only spans 5,[7,13] meaning that the former possesses extra-weak connections compared to the latter. In short, although it is still small enough to harbor a high graph density, the macaque brain is in fact about twice the size of the marmoset brain and is already on its way to partial disconnection.[7]

From a different perspective, Markov et al.[14] showed that FB connections decay with white matter distance more slowly than FF ones. This means that, on average, long-range, weak connections will tend to be FB. Extrapolating across species, we should expect the brain to become increasingly FB dominated as it grows larger, at least in primates. This aligns well with the data shown in Figure 2B, where the mean SLN value for the macaque is 0.47, which is non-negligibly lower than the 0.59 of the marmoset, meaning that the macaque is, on average, more FB than the marmoset. Given the implementation of the CIB[30] in our system, FB connections target the inhibitory population C, meaning that connectivity that is, on average, more FB will lead to greater global inhibition. This is consistent with the macaque being resilient, as the random distractor will enter a system that is, in effect, less suited to its propagation. Conversely, the marmoset system is well suited to welcome the next distractor, with its global feedforwardness more readily carrying its excitatory influence to all areas.

Circling back to the macaque FEF and DP, these are arguably the deeper reasons why they fail to display high activity. A larger brain leads to some amount of disconnection—weaker connections or even missing ones—and greater feedbackness. This, in turn, leads to less cumulated input—although more selective—for these areas. Thus, a conjecture could be that the same model grounded on a larger brain's connectivity, such as that of the human primate or other great apes, would see further disconnections and greater feedbackness, leading to more areas behaving like this. This, in turn, would be consistent with the increasingly

well-segregated subnetworks and functions that we see appear in larger brains.[18,63]

Reversing distraction and resilience is consistent with a bifurcation in highly non-linear dynamical systems

As we saw in Figures 4 and 6, this system produces, by default, a macaque resilient to distraction and a marmoset sensitive to it, on par with the behavioral data available at this time.[46,48] The anatomical frontoparietal differences between the macaque and the marmoset, such as the missing connection between the consensus marmoset areas A46D and LIP, known to be highly relevant for WM in the macaque,[26] fail to explain the difference in behavior within the constraints of our model. Even the complete swapping of species-specific connections from one to the other cannot achieve the intended behavioral reversal (Figure S8). This argues for the existence of an emergent stability produced by a network-based complex system of non-linear interactions.

This stable default behavior can nonetheless be changed by regionally (i.e., DLPFC vs. PPC) altering the connectivity. The macaque becomes distractible by artificially scaling down the prefrontal self-connectivity, in line with previous work,[39] thus effectively making it less efficient at self-activation and less prone to down-regulating parietal areas. This is consistent with experimental data, where prefrontal lesions increase distractibility in macaques.[33] In graph theoretical terms, it reduces the prefrontal's modularity. Because this alone is enough to allow a distractor to spread to all areas, this result can be interpreted as making the prefrontal more permeable to upward signals from the parietal cortex.

In the marmoset's case, both intrafrontal and frontoparietal connections need to be tuned up to achieve resilience, which, at a conceptual level, creates a continuum between the two species. However, the opposition is imperfect. Were it to be perfect, an intrafrontal increase would have been enough to render the marmoset resilient. In practice, one also needs to increase the frontoparietal connections (ρ_2) by a similar amount to complete the transition, as is shown in Figure 6B. Increasing the ρ_1 to 1.4 but keeping ρ_2 at 1 leads to a mixed regime where prefrontal areas are resilient but parietal areas remain sensitive to distractors (Figure S9C). The likely interpretation is that, by increasing only intrafrontal connections, each prefrontal area now receives enough input from its prefrontal neighbors that their collective activity is self-sustained and hard to break. We know from Murray et al.[39] that resilience to distraction is given by the prefrontal module. For it to propagate to the rest of the system, one needs to increase the influence of prefrontal areas on the parietal area, which is here modeled by increasing ρ_2.

This need to raise ρ_2 to complete the transition may come from the missing connections between marmoset area 46 (here A46D) and parietal areas LIP, OPt, and PE_PEC (Figure 3B), given the importance of area 46 to WM.[26] Although the marmoset possesses weak frontoparietal connections from A10 to the medial parietal cortex that the macaque does not (Figure 3B), these are unlikely to provide robust top-down control. Many "grafting" experiments were tried in the course of this study, but no single particular change in the matrix gave a clear-cut answer. Incidentally, this is also true with respect to both SLNs and spine count interchanges. All these results are signatures of a complex system.

Now imagine the phase diagram shown in Figure 7A as a 3D energy landscape seen from above; becoming distractible here means that the wells that constitute population A and B stable points are getting shallower, with an increasingly reduced basin of attraction that can keep the system captive (i.e., the separatrix). As ρ_1 gradually decreases, so does the depth of the wells and the size of the separatrix. Thus, there is a point at which the distractor's energy is enough to escape ($\rho_1 \approx 0.64$), only to fall into the other fixed point's energy well.

The same is true for the marmoset, only reversed with respect to ρ_1. As the parameter increases (Figure 7B), the stable fixed points are gradually pulled deeper, increasing the basin of attraction in both size and gradient and making its separatrix gradually less escapable. Starting at $\rho_1 \approx 1.065$, the energy wells are too deep and/or too steep for any distractor to efficiently push the system out, and the system becomes resilient to distraction.

As can be seen in Figure 6B as well as in Figure 7, the transition between distracted and resilient regimes is fairly sharp in both species and leads to radically different qualitative results. In dynamical systems, this corresponds to the general definition of a (global) bifurcation.[64] It appears to be correct that some aspects of the high-dimensional topology of the phase spaces in Figure 7 drastically change over a very short span of ρ_1 values.

Distraction may be adaptative given the marmoset's ecological and ethological niche

From the bifurcation perspective above, it appears that macaques and marmosets effectively sit on opposite sides of a common bifurcation. From another angle, the recent work of Joyce et al.[48] has shown that marmoset DLPFC parvalbumin neurons have a higher density of D1 (dopamine) receptors, which leads in their modeling to heightened susceptibility to distraction. Further, those levels increase from humans to marmosets, which in turn have similar levels to mice.

Therefore, beyond the brain size effect that we mentioned earlier and its link to increased feedbackness, sufficient segregation of functions, and higher cognitive capabilities,[18] this greater dopamine receptor density may indicate that heightened distractibility is in fact an adaptive trait for the marmoset. Indeed, if distraction were to be counter-selected by evolution, a reduced D1 receptor density might have been one of the easier ways to solve the issue, given the brain structural constraints at that size.

With that in mind, one can attempt a prudent link to their social ethology. Where macaques heavily rely on aggression and distrust,[65] marmosets are a highly collaborative species with respect to problem-solving, a trait otherwise fairly restricted to apes.[66,67] How would a distraction-resilient individual perform in the more collaborative social structure of marmosets? Conversely, in a strict hierarchy of aggression, would a marmoset-like macaque manage to thrive? It seems reasonable to think that distraction and social structure should present an interaction, perhaps even generate selection pressures. Future modeling of the highly non-linear evolutionary dynamics at play in this particular case could tell much about these types of interactions.

Conclusion

After producing a consensus mapping between macaque and marmoset atlases, we reduced each to a homolog parcellation scheme, thus allowing direct, area-to-area comparison of their respective connectomes. We then used these consensus data to differentially constrain an otherwise identical large-scale model of WM. Selecting for the frontoparietal WM network of the same 11 common consensus areas in the two species, we first showed that these two systems produce sustainable activity throughout the network after a cue is sent in. We went on to test their resilience to distraction and discovered that, although the macaque-constrained model resists distraction easily, the marmoset model readily switches and commits the newest cue to memory by propagating it to all areas, taking over as the new sustained activity. Moreover, the two species can be bridged by scaling up or down specific quadrants of their connectivity matrix, which effectively alters intrafrontal and frontoparietal influence over the system, allowing us to better understand the differences between those two primates. We argue that these behavioral differences between models align intriguingly well with real-life behavioral differences and offer a credible prediction of the marmoset's behavior in this specific task.

Limitations of the study

With respect to scaling up the model to 29 areas (Figures S7D and S7E), the enhanced stability given by the sheer number of areas forbids even the marmoset model from being sensitive to distraction. This points to a limitation of this multiregional model, which, due to its architecture, tends to already be resilient to distraction in two areas.[39] The consequence is that the marmoset's 11 area model distractibility is very much non-trivial. As scaling up the number of areas tends to lead to resilience from distraction, it means that there is something very specific about the marmoset WM subnetwork's anatomy that manages to prevent said resilience.

It is only fair to recognize that we have, at this date, less available spine count data for the marmoset than we currently do for the macaque (Table S1 vs. Table S2; for non-consensus data, see Theodoni et al.[7]). Therefore, if the models are indeed identical across our two species, the marmoset may be considered at this point less constrained than the macaque. New data or data updates in the future may very well change the present results by making them more alike or more different, by reducing the window of distractibility of G or by expanding it. New macaque data could possibly create a band of distractibility on the G parameter line. This point, incidentally, is just as true for any change in the connectivity.

Furthermore, as compelling as the proposed hypothetical link between anatomy and behavior may be, it cannot possibly be the entire story. Indeed, many other explanatory factors are, by necessity, at work in the production of this behavioral difference, from microcircuits to other anatomical gradients, neuronal subtypes, electrophysiology, etc. What this study shows is that the differential anatomy between those two species, at least in the subnetwork of WM, does predict some behavioral difference with respect to the presence of distractors, which appears to be coherent with the behavioral differences so far known to experimentalists working on these species. Future work in large-scale modeling, as well as modeling of evolutionary dynamics, will need to incorporate increasingly finer-grained details of neurophysiology in order to fully disentangle the links between structure and function.

RESOURCE AVAILABILITY

Lead contact

Requests for further information and resources should be directed to and will be fulfilled by the lead contact, Xiao-Jing Wang (xjwang@nyu.edu).

Materials availability

This study did not generate new materials.

Data and code availability

- Complete consensus meso-connectome data have been deposited at Zenodo under https://doi.org/10.5281/zenodo.15612783 and are publicly available as of the date of publication.
- The original code has been deposited at Zenodo under https://doi.org/10.5281/zenodo.15612783 and is publicly available as of the date of publication.
- Videos S1 and S2 have been deposited at Zenodo under https://doi.org/10.5281/zenodo.15612783 and are publicly available as of the date of publication.
- Any additional information required to reanalyze the data reported in this paper is available from the lead contact upon request.

ACKNOWLEDGMENTS

The authors would like to thank Jorge Mejias for providing the base code and helpful advice along the way and the Wang lab for the constant challenges and discussions that helped build this paper, in particular Aldo Battista and Wayne Soo for so gracefully teaching their impressive mathematical knowledge. We would also like to thank Seán Froudist-Walsh and Mary Kate P. Joyce for the helpful discussions on the marmoset neurophysiology and behavior. This work was made possible thanks to NSF NeuroNex grant 2015276 to A.F.T.A. and X.-J.W., NIH grant R01MH062349 to X.-J.W., Simons Foundation grant 543057SPI to X.-J.W., National Health and Medical Research Council grant APP1194206 to M.G.P.R., and Australian Research Council grants DP210101042 and DP210103865 to M.G.P.R.

AUTHOR CONTRIBUTIONS

Conceptualization, L.M., P.T., M.G.P.R., and X.-J.W.; methodology, L.M., P.T., M.G.P.R., and X.-J.W.; software, L.M.; validation, L.M., P.T., M.G.P.R., and X.-J.W.; formal analysis, L.M.; investigation, L.M., P.T., A.F.T.A., and X.-J.W.; resources, L.M., M.G.P.R., and X.-J.W.; writing – original draft, L.M.; writing – review & editing, all authors; visualization, L.M. and P.T.; supervision, X.-J.W.; funding acquisition, A.F.T.A., M.G.P.R., and X.-J.W.

DECLARATION OF INTERESTS

The authors declare no competing interests.

STAR★METHODS

Detailed methods are provided in the online version of this paper and include the following:

- KEY RESOURCES TABLE
- METHOD DETAILS
  - Anatomical connectivity data
  - Spine count gradient
  - Consensus mapping: Atlas
  - Consensus mapping: Computing connectivity
  - Consensus mapping: Spine count gradient
  - Consensus mapping: 11 × 11 matrices

- Computational model: Local circuit
- Computational model: Spine count gradient as synaptic strength
- Computational model: Inter-areal connectivity
- QUANTIFICATION AND STATISTICAL ANALYSIS
  - Connectome statistics and SLN-based hierarchy

SUPPLEMENTAL INFORMATION

Supplemental information can be found online at https://doi.org/10.1016/j.celrep.2025.116847.

Received: March 17, 2025
Revised: October 31, 2025
Accepted: December 10, 2025
Published: January 14, 2026

REFERENCES

1. Sporns, O., Tononi, G., and Kötter, R. (2005). The human connectome: a structural description of the human brain. PLoS Comput. Biol. *1*, e42.
2. Hagmann, P. (2005). From Diffusion Mri to Brain Connectomics (Ph.D. thesis École Polytechnique Fédérale de Lausanne (EPFL)).
3. Harris, K.D., and Mrsic-Flogel, T.D. (2013). Cortical connectivity and sensory coding. Nature *503*, 51–58.
4. Binzegger, T., Douglas, R.J., and Martin, K.A.C. (2009). Topology and dynamics of the canonical circuit of cat v1. Neural Netw. *22*, 1071–1078.
5. Binzegger, T., Douglas, R.J., and Martin, K.A.C. (2004). A quantitative map of the circuit of cat primary visual cortex. J. Neurosci. *24*, 8441–8453.
6. Douglas, R.J., Martin, K.A.C., and Whitteridge, D. (1989). A canonical microcircuit for neocortex. Neural Comput. *1*, 480–488.
7. Theodoni, P., Majka, P., Reser, D.H., Wójcik, D.K., Rosa, M.G.P., and Wang, X.J. (2021). Structural attributes and principles of the neocortical connectome in the marmoset monkey. Cereb. Cortex *32*, 15–28.
8. Majka, P., Bai, S., Bakola, S., Bednarek, S., Chan, J.M., Jermakow, N., Passarelli, L., Reser, D.H., Theodoni, P., Worthy, K.H., et al. (2020). Open access resource for cellular-resolution analyses of corticocortical connectivity in the marmoset monkey. Nat. Commun. *11*, 1133.
9. Dorkenwald, S., McKellar, C.E., Macrina, T., Kemnitz, N., Lee, K., Lu, R., Wu, J., Popovych, S., Mitchell, E., Nehoran, B., et al. (2022). Flywire: online community for whole-brain connectomics. Nat. Methods *19*, 119–128.
10. Scheffer, L.K., Xu, C.S., Januszewski, M., Lu, Z., Takemura, S.y., Hayworth, K.J., Huang, G.B., Shinomiya, K., Maitlin-Shepard, J., Berg, S., et al. (2020). A connectome and analysis of the adult drosophila central brain. eLife *9*, e57443.
11. Harris, J.A., Mihalas, S., Hirokawa, K.E., Whitesell, J.D., Choi, H., Bernard, A., Bohn, P., Caldejon, S., Casal, L., Cho, A., et al. (2019). Hierarchical organization of cortical and thalamic connectivity. Nature *575*, 195–202.
12. Gămănuț, R., Kennedy, H., Toroczkai, Z., Ercsey-Ravasz, M., Van Essen, D.C., Knoblauch, K., and Burkhalter, A. (2018). The mouse cortical connectome, characterized by an ultra-dense cortical graph, maintains specificity by distinct connectivity profiles. Neuron *97*, 698–715.e10.
13. Markov, N.T., Ercsey-Ravasz, M.M., Ribeiro Gomes, A.R., Lamy, C., Magrou, L., Vezoli, J., Misery, P., Falchier, A., Quilodran, R., Gariel, M.A., et al. (2014). A weighted and directed interareal connectivity matrix for macaque cerebral cortex. Cereb. Cortex *24*, 17–36.
14. Markov, N.T., Vezoli, J., Chameau, P., Falchier, A., Quilodran, R., Huissoud, C., Lamy, C., Misery, P., Giroud, P., Ullman, S., et al. (2014). Anatomy of hierarchy: feedforward and feedback pathways in macaque visual cortex. J. Comp. Neurol. *522*, 225–259.
15. Felleman, D.J., and Van Essen, D.C. (1991). Distributed hierarchical processing in the primate cerebral cortex. Cereb. Cortex *1*, 1–47.
16. Horvát, S., Gămănuț, R., Ercsey-Ravasz, M., Magrou, L., Gămănuț, B., Van Essen, D.C., Burkhalter, A., Knoblauch, K., Toroczkai, Z., and Kennedy, H. (2016). Spatial embedding and wiring cost constrain the functional layout of the cortical network of rodents and primates. PLoS Biol. *14*, e1002512.
17. Ercsey-Ravasz, M., Markov, N.T., Lamy, C., Van Essen, D.C., Knoblauch, K., Toroczkai, Z., and Kennedy, H. (2013). A predictive network model of cerebral cortical connectivity based on a distance rule. Neuron *80*, 184–197.
18. Magrou, L., Joyce, M.K.P., Froudist-Walsh, S., Datta, D., Wang, X.J., Martinez-Trujillo, J., and Arnsten, A.F.T. (2024). The meso-connectomes of mouse, marmoset, and macaque: network organization and the emergence of higher cognition. Cereb. Cortex *34*, bhae174.
19. Wang, X.J., and Kennedy, H. (2016). Brain structure and dynamics across scales: in search of rules. Curr. Opin. Neurobiol. *37*, 92–98.
20. Markov, N.T., Ercsey-Ravasz, M., Van Essen, D.C., Knoblauch, K., Toroczkai, Z., and Kennedy, H. (2013). Cortical high-density counterstream architectures. Science *342*, 1238406.
21. Murre, J.M., and Sturdy, D.P. (1995). The connectivity of the brain: multi-level quantitative analysis. Biol. Cybern. *73*, 529–545.
22. Wang, X.J. (2022). Theory of the multiregional neocortex: large-scale neural dynamics and distributed cognition. Annu. Rev. Neurosci. *45*, 533–560.
23. Sreenivasan, K.K., and D'Esposito, M. (2019). The what, where and how of delay activity. Nat. Rev. Neurosci. *20*, 466–481.
24. Christophel, T.B., Klink, P.C., Spitzer, B., Roelfsema, P.R., and Haynes, J.D. (2017). The distributed nature of working memory. Trends Cogn. Sci. *21*, 111–124.
25. Leavitt, M.L., Mendoza-Halliday, D., and Martinez-Trujillo, J.C. (2017). Sustained activity encoding working memories: not fully distributed. Trends Neurosci. *40*, 328–346.
26. Goldman-Rakic, P.S. (1992). Working memory and the mind. Sci. Am. *267*, 110–117.
27. Fuster, J.M., and Alexander, G.E. (1971). Neuron activity related to short-term memory. Science *173*, 652–654.
28. Wang, X.J. (2001). Synaptic reverberation underlying mnemonic persistent activity. Trends Neurosci. *24*, 455–463.
29. Wang, X.J. (2021). 50 years of mnemonic persistent activity: quo vadis? Trends Neurosci. *44*, 888–902.
30. Mejias, J.F., and Wang, X.J. (2022). Mechanisms of distributed working memory in a large-scale network of macaque neocortex. eLife *11*, e72136.
31. Froudist-Walsh, S., Xu, T., Niu, M., Rapan, L., Zhao, L., Margulies, D.S., Zilles, K., Wang, X.J., and Palomero-Gallagher, N. (2023). Gradients of neurotransmitter receptor expression in the macaque cortex. Nat. Neurosci. *26*, 1281–1294.
32. Chafee, M.V., and Goldman-Rakic, P.S. (1998). Matching patterns of activity in primate prefrontal area 8a and parietal area 7ip neurons during a spatial working memorytask. J. Neurophysiol. *79*, 2919–2940.
33. Suzuki, M., and Gottlieb, J. (2013). Distinct neural mechanisms of distractor suppression in the frontal and parietal lobe. Nat. Neurosci. *16*, 98–104.
34. Olesen, P.J., Macoveanu, J., Tegnér, J., and Klingberg, T. (2007). Brain activity related to working memory and distraction in children and adults. Cereb. Cortex *17*, 1047–1054.
35. Lorenc, E.S., Mallett, R., and Lewis-Peacock, J.A. (2021). Distraction in visual working memory: Resistance is not futile. Trends Cogn. Sci. *25*, 228–239.
36. Bisley, J.W., and Goldberg, M.E. (2006). Neural correlates of attention and distractibility in the lateral intraparietal area. J. Neurophysiol. *95*, 1696–1717.

37. Lennert, T., and Martinez-Trujillo, J. (2011). Strength of response suppression to distracter stimuli determines attentional-filtering performance in primate prefrontal neurons. Neuron *70*, 141–152.

38. Qi, X.L., Katsuki, F., Meyer, T., Rawley, J.B., Zhou, X., Douglas, K.L., and Constantinidis, C. (2010). Comparison of neural activity related to working memory in primate dorsolateral prefrontal and posterior parietal cortex. Front. Syst. Neurosci. *4*, 12.

39. Murray, J.D., Jaramillo, J., and Wang, X.J. (2017). Working memory and decision-making in a frontoparietal circuit model. J. Neurosci. *37*, 12167–12186.

40. Prins, N.W., Pohlmeyer, E.A., Debnath, S., Mylavarapu, R., Geng, S., Sanchez, J.C., Rothen, D., and Prasad, A. (2017). Common marmoset (callithrix jacchus) as a primate model for behavioral neuroscience studies. J. Neurosci. Methods *284*, 35–46.

41. Mitchell, J.F., and Leopold, D.A. (2015). The marmoset monkey as a model for visual neuroscience. Neurosci. Res. *93*, 20–46.

42. Okano, H., Hikishima, K., Iriki, A., and Sasaki, E. (2012). The common marmoset as a novel animal model system for biomedical and neuroscience research applications. Semin. Fetal Neonatal Med. *17*, 336–340.

43. Reser, D.H., Burman, K.J., Yu, H.H., Chaplin, T.A., Richardson, K.E., Worthy, K.H., and Rosa, M.G.P. (2013). Contrasting patterns of cortical input to architectural subdivisions of the area 8 complex: a retrograde tracing study in marmoset monkeys. Cereb. Cortex *23*, 1901–1922.

44. Spinelli, S., Pennanen, L., Dettling, A.C., Feldon, J., Higgins, G.A., and Pryce, C.R. (2004). Performance of the marmoset monkey on computerized tasks of attention and working memory. Brain Res. Cogn. Brain Res. *19*, 123–137.

45. Wong, R.K., Selvanayagam, J., Johnston, K.D., and Everling, S. (2023). Delay-related activity in marmoset prefrontal cortex. Cereb. Cortex *33*, 3523–3537.

46. Nakamura, K., Koba, R., Miwa, M., Yamaguchi, C., Suzuki, H., and Takemoto, A. (2018). A method to train marmosets in visual working memory task and their performance. Front. Behav. Neurosci. *12*, 46.

47. Zlatkina, V., Frey, S., and Petrides, M. (2024). Monitoring of nonspatial information within working memory in the common marmoset (callithrix jacchus). Cereb. Cortex *34*, bhae444.

48. Joyce, M.K.P., Ivanov, T.G., Krienen, F.M., Mitchell, J.F., Ma, S., Inoue, W., Nandy, A.S., Datta, D., Duque, A., Arellano, J.I., et al. (2025). Higher dopamine d1 receptor expression in prefrontal parvalbumin neurons underlies higher distractibility in marmosets versus macaques. Commun. Biol. *8*, 974.

49. Markov, N.T., Misery, P., Falchier, A., Lamy, C., Vezoli, J., Quilodran, R., Gariel, M.A., Giroud, P., Ercsey-Ravasz, M., Pilaz, L.J., et al. (2011). Weight consistency specifies regularities of macaque cortical networks. Cereb. Cortex *21*, 1254–1272.

50. Vezoli, J., Magrou, L., Goebel, R., Wang, X.J., Knoblauch, K., Vinck, M., and Kennedy, H. (2021). Cortical hierarchy, dual counterstream architecture and the importance of top-down generative networks. Neuroimage *225*, 117479.

51. Delhaye, B.P., Long, K.H., and Bensmaia, S.J. (2018). Neural basis of touch and proprioception in primate cortex. Compr. Physiol. *8*, 1575–1602.

52. Chaudhuri, R., Knoblauch, K., Gariel, M.A., Kennedy, H., and Wang, X.J. (2015). A large-scale circuit mechanism for hierarchical dynamical processing in the primate cortex. Neuron *88*, 419–431.

53. Wong, K.F., and Wang, X.J. (2006). A recurrent network mechanism of time integration in perceptual decisions. J. Neurosci. *26*, 1314–1328.

54. Bisley, J.W., and Goldberg, M.E. (2003). Neuronal activity in the lateral intraparietal area and spatial attention. Science *299*, 81–86.

55. Jacob, S.N., and Nieder, A. (2014). Complementary roles for primate frontal and parietal cortex in guarding working memory from distractor stimuli. Neuron *83*, 226–237.

56. Moeller, S., Nallasamy, N., Tsao, D.Y., and Freiwald, W.A. (2009). Functional connectivity of the macaque brain across stimulus and arousal states. J. Neurosci. *29*, 5897–5909.

57. Flavell, S.W., Gogolla, N., Lovett-Barron, M., and Zelikowsky, M. (2022). The emergence and influence of internal states. Neuron *110*, 2545–2570.

58. Greene, A.S., Horien, C., Barson, D., Scheinost, D., and Constable, R.T. (2023). Why is everyone talking about brain state? Trends Neurosci. *46*, 508–524.

59. Kringelbach, M.L., and Deco, G. (2020). Brain states and transitions: insights from computational neuroscience. Cell Rep. *32*, 108128.

60. Froudist-Walsh, S., Bliss, D.P., Ding, X., Rapan, L., Niu, M., Knoblauch, K., Zilles, K., Kennedy, H., Palomero-Gallagher, N., and Wang, X.J. (2021). A dopamine gradient controls access to distributed working memory in the large-scale monkey cortex. Neuron *109*, 3500–3520.e13.

61. Ringo, J.L. (1991). Neuronal interconnection as a function of brain size. Brain Behav. Evol. *38*, 1–6.

62. Changeux, J.P., Goulas, A., and Hilgetag, C.C. (2021). A connectomic hypothesis for the hominization of the brain. Cereb. Cortex *31*, 2425–2449.

63. Du, J., DiNicola, L.M., Angeli, P.A., Saadon-Grosman, N., Sun, W., Kaiser, S., Ladopoulou, J., Xue, A., Yeo, B.T.T., Eldaief, M.C., and Buckner, R.L. (2024). Organization of the human cerebral cortex estimated within individuals: networks, global topography, and function. J. Neurophysiol. *131*, 1014–1082.

64. Blanchard, P., Devaney, R., and Hall, G. (2012). Differential Equations (Cengage Learning).

65. Balasubramaniam, K.N., Dittmar, K., Berman, C.M., Butovskaya, M., Cooper, M.A., Majolo, B., Ogawa, H., Schino, G., Thierry, B., and De Waal, F.B.M. (2012). Hierarchical steepness, counter-aggression, and macaque social style scale. Am. J. Primatol. *74*, 915–925.

66. Sehner, S., Willems, E.P., Vinicus, L., Migliano, A.B., van Schaik, C.P., and Burkart, J.M. (2022). Problem-solving in groups of common marmosets (callithrix jacchus): more than the sum of its parts. PNAS Nexus *1*, pgac168.

67. Miller, C.T., Freiwald, W.A., Leopold, D.A., Mitchell, J.F., Silva, A.C., and Wang, X. (2016). Marmosets: a neuroscientific model of human social behavior. Neuron *90*, 219–233.

68. Elston, G.N., Benavides-Piccione, R., Elston, A., Manger, P.R., and DeFelipe, J. (2011). Pyramidal cells in prefrontal cortex of primates: marked differences in neuronal structure among species. Front. Neuroanat. *5*, 2.

69. Elston, G.N., Oga, T., Okamoto, T., and Fujita, I. (2010). Spinogenesis and pruning from early visual onset to adulthood: an intracellular injection study of layer iii pyramidal cells in the ventral visual cortical pathway of the macaque monkey. Cereb. Cortex *20*, 1398–1408.

70. Elston, G.N., Oga, T., and Fujita, I. (2009). Spinogenesis and pruning scales across functional hierarchies. J. Neurosci. *29*, 3271–3275.

71. Elston, G.N., and Rockland, K.S. (2002). The pyramidal cell of the sensorimotor cortex of the macaque monkey: phenotypic variation. Cereb. Cortex *12*, 1071–1078.

72. Elston, G.N. (2001). Interlaminar differences in the pyramidal cell phenotype in cortical areas 7m and stp (the superior temporal polysensory area) of the macaque monkey. Exp. Brain Res. *138*, 141–152.

73. Elston, G.N., Benavides-Piccione, R., and DeFelipe, J. (2001). The pyramidal cell in cognition: a comparative study in human and monkey. J. Neurosci. *21*, RC163.

74. Elston, G.N., and Rosa, M.G. (1998). Complex dendritic fields of pyramidal cells in the frontal eye field of the macaque monkey: comparison with parietal areas 7a and lip. Neuroreport *9*, 127–131.

75. Elston, G.N., Tweedale, R., and Rosa, M.G. (1999). Cortical integration in the visual system of the macaque monkey: large-scale morphological differences in the pyramidal neurons in the occipital, parietal and temporal lobes. Proc. Biol. Sci. *266*, 1367–1374.

76. Elston, G.N., and Rosa, M.G. (1998). Morphological variation of layer iii pyramidal neurones in the occipitotemporal pathway of the macaque monkey visual cortex. Cereb. Cortex *8*, 278–294.

77. Elston, G.N., and Rosa, M.G. (1997). The occipitoparietal pathway of the macaque monkey: comparison of pyramidal cell morphology in layer iii of functionally related cortical visual areas. Cereb. Cortex *7*, 432–452.

78. Oga, T., Aoi, H., Sasaki, T., Fujita, I., and Ichinohe, N. (2013). Postnatal development of layer iii pyramidal cells in the primary visual, inferior temporal, and prefrontal cortices of the marmoset. Front. Neural Circuits *7*, 31.

79. Sasaki, T., Aoi, H., Oga, T., Fujita, I., and Ichinohe, N. (2015). Postnatal development of dendritic structure of layer iii pyramidal neurons in the medial prefrontal cortex of marmoset. Brain Struct. Funct. *220*, 3245–3258.

80. Elston, G.N., Tweedale, R., and Rosa, M.G. (1999). Cellular heterogeneity in cerebral cortex: a study of the morphology of pyramidal neurones in visual areas of the marmoset monkey. J. Comp. Neurol. *415*, 33–51.

81. Elston, G.N. (2007). Specialization of the neocortical pyramidal cell during primate evolution. Evol. Nervous Syst. *4*, 191–242.

82. Gajwani, M., Oldham, S., Pang, J.C., Arnatkevičiūtė, A., Tiego, J., Bellgrove, M.A., and Fornito, A. (2023). Can hubs of the human connectome be identified consistently with diffusion mri? Netw. Neurosci. *7*, 1326–1350.

83. Consagra, W., Venkataraman, A., and Zhang, Z. (2022). Optimized diffusion imaging for brain structural connectome analysis. IEEE Trans. Med. Imaging *41*, 2118–2129.

84. Donahue, C.J., Sotiropoulos, S.N., Jbabdi, S., Hernandez-Fernandez, M., Behrens, T.E., Dyrby, T.B., Coalson, T., Kennedy, H., Knoblauch, K., Van Essen, D.C., and Glasser, M.F. (2016). Using diffusion tractography to predict cortical connection strength and distance: a quantitative comparison with tracers in the monkey. J. Neurosci. *36*, 6758–6770.

85. Palmer, S.M., and Rosa, M.G.P. (2006). Quantitative analysis of the corticocortical projections to the middle temporal area in the marmoset monkey: evolutionary and functional implications. Cereb. Cortex *16*, 1361–1375.

86. Burman, K.J., Bakola, S., Richardson, K.E., Reser, D.H., and Rosa, M.G.P. (2014). Patterns of cortical input to the primary motor area in the marmoset monkey. J. Comp. Neurol. *522*, 811–843.

87. Burman, K.J., Bakola, S., Richardson, K.E., Reser, D.H., and Rosa, M.G.P. (2014). Patterns of afferent input to the caudal and rostral areas of the dorsal premotor cortex (6dc and 6dr) in the marmoset monkey. J. Comp. Neurol. *522*, 3683–3716.

88. Falchier, A., Clavagnier, S., Barone, P., and Kennedy, H. (2002). Anatomical evidence of multimodal integration in primate striate cortex. J. Neurosci. *22*, 5749–5759.

89. Barone, P., Batardiere, A., Knoblauch, K., and Kennedy, H. (2000). Laminar distribution of neurons in extrastriate areas projecting to visual areas v1 and v4 correlates with the hierarchical rank and indicates the operation of a distance rule. J. Neurosci. *20*, 3263–3281.

90. Nimchinsky, E.A., Sabatini, B.L., and Svoboda, K. (2002). Structure and function of dendritic spines. Annu. Rev. Physiol. *64*, 313–353.

91. Van Essen, D.C., and Maunsell, J.H.R. (1983). Hierarchical organization and functional streams in the visual cortex. Trends Neurosci. *6*, 370–375.

92. Rockland, K.S., and Pandya, D.N. (1979). Laminar origins and terminations of cortical connections of the occipital lobe in the rhesus monkey. Brain Res. *179*, 3–20.

93. Paxinos, G., Watson, C., Petrides, M., Rosa, M., and Tokuno, H. (2012). The Marmoset Brain in Stereotaxic Coordinates (Elsevier Academic Press).

94. Solomon, S.G., and Rosa, M.G.P. (2014). A simpler primate brain: the visual system of the marmoset monkey. Front. Neural Circuits *8*, 96.

95. Bakola, S., Burman, K.J., and Rosa, M.G.P. (2015). The cortical motor system of the marmoset monkey (callithrix jacchus). Neurosci. Res. *93*, 72–81.

96. Abbott, L.F., and Chance, F.S. (2005). Drivers and modulators from push-pull and balanced synaptic input. Prog. Brain Res. *149*, 147–155.

97. Tsushima, Y., Sasaki, Y., and Watanabe, T. (2006). Greater disruption due to failure of inhibitory control on an ambiguous distractor. Science *314*, 1786–1788.

98. Hupé, J.M., James, A.C., Payne, B.R., Lomber, S.G., Girard, P., and Bullier, J. (1998). Cortical feedback improves discrimination between figure and background by v1, v2 and v3 neurons. Nature *394*, 784–787.

99. Girard, P., and Bullier, J. (1989). Visual activity in area v2 during reversible inactivation of area 17 in the macaque monkey. J. Neurophysiol. *62*, 1287–1302.

100. Lesnoff, M., and Lancelot, R. (2024). aods3: Analysis of Overdispersed Data using S3 Methods. https://CRAN.R-project.org/package=aods3rpackageversion0.5.

STAR★METHODS

KEY RESOURCES TABLE

REAGENT or RESOURCE	SOURCE	IDENTIFIER
Deposited data		
Macaque 40 area connectivity data	Henry Kennedy[60]	core-nets.org
Marmoset 55 area connectivity data	Marcello Rosa[8]	analytics.marmosetbrain.org
Consensus macaque 35 area connectivity data	This paper	https://doi.org/10.5281/zenodo.15612783
Consensus marmoset 45 area connectivity data	This paper	https://doi.org/10.5281/zenodo.15612783
Kennedy lab injection Metadata	Henry Kennedy (Markov et al.[13]; Table S2)	https://oup.silverchair-cdn.com/oup/backfile/Content_public/Journal/cercor/24/1/10.1093_cercor_bhs270/1/bhs270_Supplementary_Data.zip?Expires=1758568837&Signature=tuS7VgSafvR9Y7bDZ~YWfVtYdIOL8iy0oFaink2iHNmf-N02kSxIJ~xYm-IJBkSoZfV5VuzZyXlw0Ts1114gR2p1yUHpXixcKlJKvncqWDE4amv6xbNotYaU00YF76352YHxrfoHeOpbL-3K-HHgPiownvZ~0o6so-b4ExkG4sqLJljl~7ITi5VCm405R7Umbrrjku9EuBQUTXrryaIKgG-PjmCzZYv-~z1vo3N12MFRJw8loPsdrhVj1NGj8IQqA0fxkY7syYAPu2usONGtDywCpvPr1qz3ZHaIJWMVBHwA9Q8~YYWczg1qPNEG8LiGtTWeUlj2oE7ylNhNYdunLw__&Key-Pair-Id=APKAIE5G5CRDK6RD3PGA
Rosa lab injection metadata	Marcello Rosa (Theodoni et al.[7]; Tables S1–S3)	https://oup.silverchair-cdn.com/oup/backfile/Content_public/Journal/cercor/32/1/10.1093_cercor_bhab191/2/supplementary_rereview_may2021_bhab191.zip?Expires=1758569354&Signature=ecXPnCRIyEuVDXkKMn7IWasMweUQW0FR1g1cM~0DmXNrNGNsihiVLyFlc3qiFYF8UUit6DZVQFrB2jVGOiarJLHCpYW3i~IGGB8bdXKzx4eWrqINEtubAxLf~fQl0hs4T4AlNJ0GHgAyv4KnZ3n~X4U1ey0an-1dcS3ahT1vMyUCxhhfU~b7GRzPMg42K86juHoPmdu6IXfmShsOUUDFf67F9DwLHD8hQVGsQDYpdAZy2mwHs0M-hUwF6CewUqYAI7neIPdb2YZg75dbWYMCMH8jB-HG6m3Ywd3REQNTAakxwRMafNKIW3FbfNSZLd0TbvfV-3jS93qwscHtOTHUEQ__&Key-Pair-Id=APKAIE5G5CRDK6RD3PGA
Macaque spine count data	Guy Elston (Elston et al.[68–70]; Elston and Rockland[71]; Elston[72]; Elston et al[73]; Elston and Rosa[74]; Elston et al[75]; Elston and Rosa[76,77])	N/A
Marmosey spine count data	Noritaka Ichinohe; Guy Elston (Oga et al.[78]; Sasaki et al.[79]; Elston et al.[80,81])	N/A
Consensus macaque spine count data	This paper	Table S1
Consensus marmoset spine count data	This paper	Table S2
Software and algorithms		
Large-scale dynamical model simulation and analysis code	This paper	https://doi.org/10.5281/zenodo.15612783
Julia programming language	Julia	julialang.org
R programming language	The R Project	www.r-project.org

METHOD DETAILS

Anatomical connectivity data

Despite the continuous progress occurring in the field of diffusion MRI and tractography based connectomics,[82,83] it nonetheless remains true that, where feasible, retrograde tract-tracing experiments still constitute the gold standard in cortical

connectivity/mesoscale connectomics.[84] In the realm of primates, we are now uniquely suited to tackle cross-species comparison as extensive databases have been produced in both the macaque[13,60] downloadable from core-nets.org, the historical model in primate neuroscience, and now the marmoset[7,8] downloadable from analytics.marmosetbrain.org, a smaller primate model that is easier to handle whilst retaining many primate features important to today's neuroscience.

Injections of retrograde tracers are carried out in multiple areas, designated as "target" areas, over multiple experiments. Each injection site is controlled so that the injection covers all 6 layers of the cortex, whilst not infringing on the white matter, so that the dye is not captured by fibers of passage. At the injection site, the dye is captured by axon terminals and is actively transported backward toward the soma of the cell, thus only labeling neurons that directly project onto the injection site (Figure S1A). These neurons are subsequently detectable through fluorescent microscopy. Tracers here employed are monosynaptic, meaning that they cannot continue their course beyond the one neuron that captured them into another neuron that shares a synapse with the back-labeled cell.

Many of the injected areas in both species are represented only by a single injection. It has been shown that the connectivity patterns of repeated injections are remarkably stable across individuals for injections in V1, V2 and V4 for retinotopically equivalent points in each of those areas[49] (in this case foveal). The same observation had already been made for marmoset visual area MT.[85] Importantly, in both species this repeatability includes weaker projections previously unknown to the field. The same analysis was repeated in frontopolar area 10[13], on the opposite side of the brain, and in the motor cortex,[86,87] thereby proving that this repeatability is not a feature restricted to the visual system. This statistical stability erodes as the parcellation scheme becomes finer and finer grained, and becomes stronger with a coarser parcellation,[13] such as our consensus mapping. This means that a single properly done injection is statistically sufficient to get an accurate and stable connectivity pattern, with repetitions providing only limited additional information. This is also reported to be true for mouse[12] and the marmoset.[7] Injection experiments metadata for both macaque and marmoset can be found through the links provided in the key resources table.

Labeled cells are counted and attributed to "source" areas according the species' parcelation atlas and their position with respect to granular layer 4 (i.e., infragranular for layer 5 and 6; supragranular for layers 2 and 3). From this data extraction are computed two basic connectivity metrics. The first one is the Fraction of Labeled Neurons (FLN[88]), defined as the number of labeled cells in a given area divided by the total number of labeled cells for the injection (i.e., in all cortical areas, excluding labeling in the injected area; Figure S1B), thus giving the relative weight of the connection. By doing so, all injections are normalized to 1, thus allowing comparison between injections. The second metric is the Supragranular Labeled Neuron (SLN[89]), defined as the number of labeled cells in the supragranular compartment of an area divided by the total number of labeled cells for that area (i.e., both infra and supragranular; Figure S1B). This metric allows us to quantify the feedforward/feedbackness of a connection, with values close to 0 being identified as feedback (FB) and values close to 1 as feedforward (FF). These SLNs can be used to produce a species specific cortical hierarchy[14,50] that has been shown to correlate with cortical gradients of several biological measurements, such as areal spine counts[30,52] or the recently discovered neurotransmitter receptor gradients.[31] Over many injections, both metrics are usually displayed as matrices, with as many rows as there are areas in the relevant atlas (here macaque or marmoset), and as many columns as there is injections. Repeated injections are summed as if they where a single massive injection, which is consistent with standard practices when dealing with repeat injections, as in Markov et al.,[13] Markov et al.[49] In practice, what will be used throughout this paper is the square matrix (i.e., where source and target areas are the same) for each of those metrics, that is the edge-complete (i.e., all connections are known) graph of all commonly injected consensus areas.

Spine count gradient

The other anatomical constraint, besides connectivity, that is applied to the model is the gradient of spine count as investigated across several publications for both macaque[68–77] and marmoset.[73,78–80] Spine counts, as captured by the total number of spine on the basal dendrites of layer 2/3 pyramidal cells, have been shown in macaques to vary across areas by more than 10-fold from 600 in V1 more than 8000 in premotor areas. Further, Nimchinsky et al.[90] showed that approximately 90% of excitatory synapses on neocortical pyramidal cells are on dendritic spines, thus making a strong argument that a greater amount of spines results in a greater excitability. Elston[81] in turn suggested that spine count differences are likely to impact local summation of postsynaptic potentials. Because of this, spine counts can be used as a proxy to the self connectivity of a population.

Additionally, it is a non trivial discovery that these spine count values correlate positively with the SLN-based cortical hierarchy for both macaque and marmoset,[7,30,52] computed from retrograde tracer connectivity where the hierarchy is statistically inferred through a beta-binomial GLM applied to the SLN values.[14,50] This conception of hierarchy is itself rooted in the anatomical understanding of FB and FF.[15,91,92] The very fact of this correlation means that the hierarchy captures an important aspect of cortical areal differences, which can be used to complete the data where missing. All spine count values and their corresponding bibliographical references are given in Tables S1 and S2, along with their hierarchical index.

Consensus mapping: Atlas

One of the key requirements of a formal comparative analysis of nervous systems is a step aimed at mapping the anatomical knowledge available for one species into registration with that available for the other. In the present study, this requirement translated into identifying homologous parcels of cerebral cortex in the marmoset and macaque, so the patterns of connectivity could be directly related within a same spatial reference frame. This process was, in practice, limited by issues related to the use of different

nomenclatures by different laboratories, data availability (e.g., the areas explored with tracer injections may not be the same in the two species), and the likelihood of genuine biological differences. To circumvent such issues, we created a consensus map that describes the subdivision of the cortex of the two species in a manner that results in identification of the same number of homologous parcels (areas, or groups of areas) for which the results of tracer injections were available (Figure 1; Table S3).

This consensus mapping provides a way to directly relate the cortical areas proposed by Paxinos et al.[93] in the marmoset, which recognizes 116 histologically distinct areas, and those proposed by Markov et al.[13] in the macaque, which recognizes 91 areas. These atlases were chosen because they were used as the basis for describing the most comprehensive cellular-level connectomic datasets available.[7,8,13,14,60] Alignment of the two parcelations was guided by several criteria, which included location in the brain and relative to other areas, histological structure, and, where available, functional data and pattern of connectivity.

In the simplest case, single areas could be directly identified in the two species using available histological and functional criteria. For example, the majority of the areas of the visual and premotor cortex could be identified with a high degree of certainty based on previous anatomical and functional studies.[94,95] In other cases, one area in one species was related to 2 or more areas in the other. For example, the marmoset caudal somatosensory cortex is not clearly differentiated into areas 1 and 2, as in the macaque, and appears instead the single area A1-2. Conversely, whereas marmoset area 3 is subdivided into A3a and A3b, the macaque atlas only provides a single subdivision called area 3. More complex mappings were required, leading to larger parcels. For example, in the macaque medial temporal lobe, area TH/TF was equated to five areas in the marmoset cortex: TF, TFO, TH, TL and TLO. At the end of this process, we are left with an consensus atlas of 75 areas. Let it here be noted that the subiculum (“SUBI” in Figure 1), entryway to the hippocampus proper and part of the hippocampal formation, is not part of the marmoset original parcelation, and therefore absent from the consensus one as well, effectively bringing down the consensus to 74 areas, since keeping the subiculum in the macaque is non consensual. Nonetheless, it was kept for completeness sake, and is not involved in the simulations reported here. The complete table of consensus equivalence across the two species is available in Table S3.

Consensus mapping: Computing connectivity

The consensus atlas now set, the connectivity of the two independent dataset must be converted to this new atlas of 74 common consensus areas, before they can be fully compared and used in a large-scale model. To do so, FLN, SLN and spine count values have to be combined so as to fit the new parcelation. As the consensus is essentially merging areas and area subdivisions together in either species to converge on homolog parcelation schemes, the connectivities of both species should reflect this by summing together source areas at the level of neuron counts. In other words, all the relevant connectivity transformations happen in the count matrices, created from the downloadable material for both species (see Method section anatomical connectivity data). It must be stressed that to do so, one needs separated neuron count matrices for infragranular and supragranular numbers for both species, and that any operation needs to happen in the same fashion in both infra and supragranular matrices for each species.

For a given injection, two source areas (i.e., two rows in the count matrix) that need to be merged will see their respective counts of neurons summed together as a single area. Additionally, two target areas (i.e., two columns in the count matrix) will also be summed together, as if it were a large unique injection. The decision to sum, as opposed to average them together, follows the same logic as with the repeat injections explained above.[13,49] It stems from the fact that computing FLNs and SLNs are linear transformations that both involve dividing by the cumulated sum across injections. Additionally, averages tend to create non integer quantities for counts, where summing does not.

Once the new count matrices are ready and conform to the consensus parcelation, the macaque original matrices of 40×91 have become 35×74 matrices under consensus. Similarly, the marmoset ones have changed from 55×116 to 45×74. Complete consensus FLN and SLN matrices can be examined in Figures S2 and S3 and full consensus data is available in Table S5. Of the 35 and 40 consensus injected areas for the macaque and the marmoset respectively, 29 are commonly injected in both species. Common consensus square *FLN* and *SLN* matrices of size 29×29 (Figures 1E, 1F, and S4) are then extracted and, in the case of *FLN*, columns are renormalized to sum to 1, so that injections are directly compatible to one another. This is a standard practice in meso-connectomics, given the variation of injected volumes tracer from one injection to the next, and the sum total of neurons being a excellent proxy for injection volume and uptake zone size.[88]

Consensus mapping: Spine count gradient

Merging spine counts to follow the consensus parcelation leads to two potential cases: either merging 2 areas (or more) that all have spine counts attributed to them prior to consensus, or merging 1 area that has a spine count with another area that does not. Through sheer happenstance, the first case never did present itself in either species, due in part to the fact that spine counts have been measured in the context of broader areas (i.e., area 46 or TE, which are larger than the currently used parcelation), and in part because far from all pre-consensus areas have been tested for spine counts. When the second case presented itself, the most parsimonious position was to assume homogeneity, and therefore attribute the spine count value of the first area to the resulting consensus area. This more parsimonious approach is further validated because spine counts are computed for an average neuron in each area.

In the case of consensus areas for which no spine count data was available prior to consensus, then the SLN-based hierarchy was used, itself computed from the consensus SLN matrices, as explained in Method section spine count gradient and computational model: Spine count gradient as synaptic strength, following the methods from Vezoli et al.[50] and Markov et al.[14]

Consensus mapping: 11 × 11 matrices

In order to study the particularities of the WM system proper, we expended the 2-compartment model of Murray et al.,[39] which modeled PPC and DLPFC with each with a single Wong-&-Wang, into an 11 area model, where PPC and DLPFC are now 6 and 5 areas, respectively. Doing so therefore encompasses all available consensus data regarding the parietofrontal network, known to be the substrate of WM.[26] These 11 × 11 matrices can be seen in Figure 3B and consist of 6 PPC and 5 DLPFC consensus areas. The corresponding spine count values were taken from the consensus spine count gradient described above in Method section consensus mapping: Spine count gradient.

Computational model: Local circuit

Conceptually, the system built here should be thought about as a network of Wong-&-Wang models,[30,53] each corresponding to a particular cortical area, and whose connectivity to other areas (i.e., other Wong-&-Wangs) are structured and constrained by the retrograde tracer connectivities described above (Figure 3A).

The local system, which belongs to the category of mean-field models, possesses in our case three explicit variables r_A, r_B and r_C, describing the temporal evolution of the firing rates of three neural populations: two excitatory (populations A and B) and one inhibitory (population C). The equation of the firing rate for each population is as follows:

$$\tau_r \frac{dr_i}{dt} = -r_i + \Phi_i(I_i) \quad \text{(Equation 1)}$$

Here, and in all future equations, all parameter values are taken from Mejias & Wang,[30] except G and ρ. The index i can be A, B or C, depending on the population. $\tau_r = 2$ ms and $\Phi_i(I_i)$ is a transfer function that converts the total current I of a population into a firing rate, according to the following equations[96]:

$$\Phi_{A,B}(I) = \frac{aI - b}{1 - exp(-d(aI - b))} \quad \text{(Equation 2)}$$

$$\Phi_C(I) = \left[\frac{1}{g_I}(c_1 I - c_0) + r_0\right]_+ \quad \text{(Equation 3)}$$

with $a = 135$ Hz/nA, $b = 54$ Hz, and coefficient $d = 0.308$ for Equation 2; and $g_I = 4$, $c_1 = 615$ Hz/nA, $c_0 = 177$ Hz and $r_0 = 5.5$ Hz for Equation 3. The index "+" in $[expr]_+$ indicates a rectification where all negative values are set to 0.

Given that Φ_i evolves as a function of I_i, let us define next the current equations for each population:

$$I_A = J_s S_A + J_c S_B + J_{EI} S_C + I_{0A} + I_{net,A} + x_A(t) \quad \text{(Equation 4)}$$

$$I_B = J_c S_A + J_s S_B + J_{EI} S_C + I_{0B} + I_{net,B} + x_B(t) \quad \text{(Equation 5)}$$

$$I_C = J_{IE} S_A + J_{IE} S_B + J_{II} S_C + I_{0C} + I_{net,C} + x_C(t) \quad \text{(Equation 6)}$$

Starting with the fixed parameters for this set of equations, the cross-coupling parameter J_c has a value of 0.0107 nA and encapsulates how the two excitatory populations A and B cross-activate each other. J_{EI} is the coupling parameter regulating the input from inhibitory population C into excitatory populations A and B. Being inhibitory, the term $J_{EI}S_C$ must be negative, so J_{EI} is set at −0.31 nA. J_{II}, population C inhibitory input onto itself, is also negative at −0.12 nA. Background current parameters I_{0A} and I_{0B} are identical and set at 0.3294 nA, I_{0C} is set at 0.26 nA.

Although fixed, the self-coupling parameter J_s and the excitatory-to-inhibitory coupling parameter J_{IE} are different for each area depending on the spine count gradient (see Method section spine count gradient) and will be explained in a dedicated section down below (Method section computational model: Spine count gradient as synaptic strength). Similarly, the $I_{net,i}$ terms for each populations, which encapsulates the role of the inter-areal anatomical connectivity (Method section anatomical connectivity data), requires its own dedicated explanations further down (Method section computational model: Inter-areal connectivity).

The variables collectively designated as S_i are described by the conductance equations below, and truly govern the local system:

$$\frac{dS_A}{dt} = -\frac{S_A}{\tau_N} + \gamma_E(1 - S_A)r_A \quad \text{(Equation 7)}$$

$$\frac{dS_B}{dt} = -\frac{S_B}{\tau_N} + \gamma_E(1 - S_B)r_B \quad \text{(Equation 8)}$$

$$\frac{dS_C}{dt} = -\frac{S_C}{\tau_G} + \gamma_I r_C \quad \text{(Equation 9)}$$

In these, S_i are the conductances for each population; the τ_N (NMDA) and τ_G (GABA) time constants are set at 60 and 5 ms respectively; and γ_E and γ_I, set at 1.282 and 2, are dimensionless saturation factors for the excitatory and inhibitory populations, respectively again. Finally, r_i is the firing rate of each population from Equation 1.

The last term in the current Equations 4, 5, and 6, $x_i(t)$, signifies an Ornstein-Uhlenbeck process, which introduces some level of stochasticity, and can be construed as random noise intrinsic to the system. It is defined be the following equation:

$$\tau_{noise}\frac{dx_i}{dt} = -x_i + \sqrt{\tau_{noise}}\sigma_i\xi_i \quad \text{(Equation 10)}$$

where τ_{noise} is the time constant for the process set at 2 ms, σ_i is the noise strength set at 0.005 nA for populations A and B, at 0 for population C. The last term ξ_i is the Gaussian white noise, on which σ_i is applied.

Finally, still in Equations 4, 5, and 6, an implicit term μ can be added to introduce sensory stimulations into the system, in which case $\mu = 0.3$ nA for a duration of 500 ms. Figure 3D shows the schematic progression of the task modeled in this study, with the cue and the distractor stages being where μ is non zero for one of the populations.

Computational model: Spine count gradient as synaptic strength

What makes large-scale models increasingly important as neuroscience progresses is their ability to incorporate differences between cortical areas, where they would otherwise be construed—and modeled—as rigorously identical units. Here, we use a brain wide gradient of spine count to uniquely constrain our system, whereby each area is characterized by a spine count value, as exposed in Method section spine count gradient, which is used to compute an area-specific self-coupling parameter J_s through the following equation:

$$J_s(a) = J_{min} + (J_{max} - J_{min})\frac{\tilde{h}_a}{\tilde{h}_{max}} \quad \text{(Equation 11)}$$

where a is a consensus area; J_{min} is the minimal synaptic strength set at 0.21 nA; and J_{max} is the maximal value synaptic strength can take, set at 0.42 nA, effectively bounding J_s between those to values. $\tilde{h}_a/\tilde{h}_{max}$ is meant to represent the normalized spine count gradient, completed by SLN-based hierarchical estimates $\widehat{h}_a$ where necessary (see Table S1). This effectively produces a gradient of J_s values, spanning from J_{min} to J_{max}. J_{max} being inferior to bifurcation threshold J^* ensures that no single area taken alone is able to achieve multistability (Figure 3C).

From J_s is computed J_{IE} with the subsequent equation:

$$J_{IE}(a) = \frac{1}{2J_{EI}\zeta}(J_0 - J_s(a) - J_c) \quad \text{(Equation 12)}$$

where a is again an area; J_c and J_{EI} are the same parameters as in Equations 4, 5, and 6, set at 0.0107 and −0.31 nA respectively. Parameter ζ is fixed on parameters previously spelled out:

$$\zeta = \frac{\tau_G\gamma_I c_1}{g_I - J_{II}\tau_G\gamma_I c_1} \quad \text{(Equation 13)}$$

with τ_G and γ_I from Equation 9; c_1 and g_I from Equation 3; and J_{II} from Equation 6. The explanation for the precise definition of ζ can be found in the methods of Mejias & Wang.[30] Briefly, the baseline activity level of each local Wong-&-Wang circuit is by default dependent on J_s, and areas with high values could exhibit spontaneous persistent activity. They could in principle even go beyond physiologically realistic limits if left unbounded. We control this by imposing on the system that all areas have the same baseline, regardless of their specific J_s value. We allowed three simplifying assumptions: The system is symmetrical with respect to populations A and B (at baseline, the only input the background current, and $I_{0A} = I_{0B}$), noise is negligible, and population C has significantly faster dynamics, as they are mediated by GABA. After simplification, Equations 12 and 13 are deduced, with J_0 being set at 0.2112 nA. The linear relationship described in Equations 11 and 12 ensures that the baseline activity is the same for all areas in the network. Note that deviations from this linear relationship would simply lead to different areas having slightly different spontaneous activity levels, but it does not substantially affect our main results.

Because J_{IE} needs to always be non negative, Equation 12 imposes a lower bound to the values J_s can take in Equation 11 at 0.205 nA. On the other side of its range, a J_s that would be higher than the bifurcation point of the system (0.4655 nA for an isolated Wong-&-Wang parametrized as described so far) would grant multistability to the system. Therefore, setting J_{max} below that bifurcation threshold ensures that all areas are monostable when taken in isolation. In other worlds, each individual area cannot on its own display sustained activity, even after a stimulation, and any persistent non baseline firing rate is strictly an effect multi-areal system as a whole. Here, as described above, setting J_{min} and J_{max} at 0.21 and 0.42 nA respectively ensures that our system displays distributed WM as a non linear effect of associating monostable areas together.

Computational model: Inter-areal connectivity

Going back to Equations 4, 5, and 6, the term $I_{net,i}$ still requires explanations. This term designates the current that, for each population in each area, comes from the rest of the network outside the area in question. Said differently, it is the global input current to each area, and is defined as such:

$$I^x_{net,A} = G\sum_y W^{xy} SLN^{xy} S^y_A \quad \text{(Equation 14)}$$

$$I^x_{net,B} = G\sum_y W^{xy} SLN^{xy} S^y_B \quad \text{(Equation 15)}$$

$$I^x_{net,C} = \frac{G}{Z}\sum_y W^{xy}(1 - SLN^{xy})(S^y_A + S^y_B) \quad \text{(Equation 16)}$$

In these, indices x and y respectively represent rows and columns of matrices W^{xy} and SLN^{xy}, where each column is a target area (i.e., injection site) and each row is a source area. Additionally, y the y^{th} element in column vector S^y_i. The summation over y applies over the expression $W^{xy} SLN^{xy} S^y_i$ (or the population C equivalent), which is the pairwise (i.e., Hadamard) product of matrices W, SLN and column vector S_i. The output of said summation is the row vector $I^x_{net,i}$, where x is the x^{th} element in the vector.

G stands for the global coupling parameter, which tunes up or down the importance of the input from the network to a given area. G has to scale down as the number of areas scales up, or the sum that is I_{net} will gradually take over the current Equations 4, 5, and 6 and the dynamics will blow up exponentially. The exact value of G is different for the two species (see Results: Standard Behavior) and are set at 0.98 and 0.85 (0.4 and 0.42 in the 2 × 2 case; 0.51 and 0.33 in the 29 × 29 case) for macaque and marmoset respectively, for all simulations. Z is a scalar that controls the balance between excitatory and inhibitory inter-areal connections. $Z = 1$ would mean that long-range excitatory and inhibitory projections are of equal strength. In our particular case, we needed to enforce the following condition: if excitatory populations A and B are both active at the same time and at the same level in a given area, then their net effect on other areas in the network should be 0. Given this imperative, parameter Z can be deduced as follows:

$$Z = \frac{2c_1\tau_G\gamma_I J_{EI}}{c_1\tau_G\gamma_I J_{II} - g_I} \quad \text{(Equation 17)}$$

with c_1 and g_I from Equation 3; τ_G and γ_I from Equation 9; J_{EI} and J_{II} from Equations 4, 5, and 6.

Back to Equations 14–16, W^{xy} is the weight matrix, which we get to through the following sequence of transformations: First we define the matrix U as the non linear rescaling of matrix FLN (see Method section anatomical connectivity data):

$$U^{xy} = k_1(FLN^{xy})^{k_2} \quad \text{(Equation 18)}$$

where k_1 and k_2 are rescaling factors of value 1.2 and 0.3 respectively. The rescaling described by Equation 18 is done so that the range of FLN values, which spans 5 to 6 orders of magnitude, is better suited to a firing rate model. The same qualitative behavior can be obtained with other k_1 and k_2 values, or even other rescaling functions, so long as a standard working regime is achieved. The values were kept from Mejias & Wang[30] for consistency.

We then renormalize U by column to obtain V:

$$V^{xy} = \frac{U^{xy}}{\sum_y U^{xy}} \quad \text{(Equation 19)}$$

Importantly, this renormalization step, named as such to differentiate it from the original normalization that produces FLNs, is to be performed only once, on the edge-complete 29 × 29 matrix. The 11 × 11 connectivity matrix of parietal and prefrontal areas is not renormalized again, as it is considered a subpart of a larger network, not its own independent system.

Finally, to obtain our true weight matrix W, the spine count gradient is introduced to the inter-areal connectivity so that global and local circuitry be of the same trend, like so:

$$W^{xy} = \frac{J_s(a)}{J_{max}} V^{xy} \quad \text{(Equation 20)}$$

Going back once more to the $I_{net,i}$ Equations 14-16, the SLN term indicates the square matrix of SLN values, already described in anatomical connectivity data. As SLN values evolves between 0 and 1, with 0 meaning FB and 1 as FF, pairwise multiplication of the SLN and the W matrices gradually filters out FBs as a function of the SLN value. If it is a reasonable assumptions that FFs should be excitatory, as it facilitates signal propagation to the entire system, having FB do the same would lead to excitatory reverberation and all areas being indiscriminately activated as well as having similar firing rates during WM delay, as shown by Mejias & Wang.[30] In the same paper, the authors introduce the notion of Counterstream Inhibitory Bias (CIB), by which the weight matrix W is, for the inhibitory population C of each area, not pairwise multiplied by SLN but by (1-SLN), thus filtering out FF connections, not FB ones. By doing so, the model effectively takes on the assumption that FBs connect to inhibitory neurons which, if it is very much consistent with the known FB modulatory effects,[97–99] the existence of such FB-to-inhibitory-cell connections still remains to be proven at the cellular level. That being said, applying the CIB to a distributed WM model does yield a pattern of sustained activity during WM that is

remarkably close to known electrophysiological data,[30] thus making the CIB a fascinating as well as credible prediction to be tested by experimentalists.

Finally, all parameters of the model are listed in Table S4.

QUANTIFICATION AND STATISTICAL ANALYSIS

Connectome statistics and SLN-based hierarchy

All Statistics were performed in R. Macaque vs. marmoset FLN correlations (Figure 2) where done using the linear model function of the *stats* package, which is part of the base sets of packages in R. The SLN-based hierarchy of each species was computed following the methods developed in Markov et al..[14,50] In short, we suppose that we can assign hierarchical levels, h_i and h_j, to all area pairs i and j, based on a the SLN measurements taken from injection in area a. Then, we assume that:

$$g\left(SLN_i^a\right) - g\left(SLN_j^a\right) = h_i - h_j \quad \text{(Equation 21)}$$

where g applies a logit or probit transformation to SLN values, from an injection into area a that receives projections from areas i and j. This suggests a formalism similar to a GLM with a binomial family. The SLN is taken as a binomial variable (neurons are found in the upper or lower cortical layers) and the sum of neurons in both compartments is used a weight. The problem can be reframed as follows:

$$g\left(SLN_i^a\right) = Xh \quad \text{(Equation 22)}$$

where X is the incidence matrix of the cortical graph, and h the vector of hierarchical values, the product of which maps the differences in hierarchical value between two areas with the differences between the transformed SLN.

A negative beta-binomial model (with a probit link function) was used, given that the distribution of the response variable, here the expected SLN values, has a greater variability than the usual binomial distribution and is better described by a beta distribution (aods3 linear model from the *aods3* R package[100]). For present purposes, the model can be reparameterized to include a dispersion parameter that better models the overdispersion typically observed in neural counts.[14] Once the statistical model is specified, the coefficients are estimated by maximum likelihood. Note that because numbers of neurons are used in the model and not just the SLN proportions, this method generates a weighted hierarchy.